Geophysical Journal International

Geophys. J. Int. (2026) **244,** 1–20
Advance Access publication 2026 January 08
Research Paper

https://doi.org/10.1093/gji/ggaf531

Partially joint petrophysical inversion

H. Söding ,[1,2] F. M. Wagner [2] and H. Maurer[1]

[1] *Institute of Geophysics, ETH Zurich, CH-8092 Zurich, Switzerland . E-mail: hagen.soeding@eaps.ethz.ch*
[2] *Geophysical Imaging and Monitoring, RWTH Aachen University, D-52062 Aachen, Germany.*

Accepted 2025 December 23. Received 2025 December 23; in original form 2025 August 5

SUMMARY

Joint petrophysical inversion is a powerful technique for using multiple geophysical modalities to estimate petrophysical or geotechnical parameters of the subsurface. A precise knowledge of the petrophysical laws for the full model domain is imperative to enable petrophysical coupling. In this work, we investigate the effect of partially invalid petrophysical laws on the inversion of a synthetic data set, using electrical resistivity tomography (ERT) and seismic traveltime data to image a CO_2 plume in a Carbon Capture and Storage (CCS) setup. We consider a model consisting of a reservoir and a caprock in which only the reservoir can be described by a petrophysical law. We first apply a conventional (joint) petrophysical inversion (JPI) and show that the use of wrong petrophysical laws leads to systemic artefacts within the parts of the model in which the petrophysical relations are invalid. We then present a new hybrid partially petrophysically coupled joint inversion (P-JPI) approach that combines petrophysical coupling for regions with valid petrophysical laws, and structural coupling, whenever no reliable petrophysical laws are available. The P-JPI approach outperforms tomography based on the individual ERT or seismic data set, as well as joint structural inversion (JSI) based on the cross-gradient functional. The partially petrophysically coupled joint inversion thus enables petrophysical coupling and provides a unique, quantitatively interpretable saturation model for the CO_2-plume. We further show that it is possible to detect zones with incorrect petrophysical relations by analysing the difference of the model updates based on the standalone data sets. Finally, we combine the detection of zones of incorrect petrophysical laws with the P-JPI to derive an inversion scheme that is independent of prior knowledge of the validity of petrophysical laws. Our novel methods facilitate direct estimation of the petrophysical subsurface parameters from multiple geophysical measurements if petrophysical relations are only available for parts of the model domain and provide means to quantify the spatial extent of regions where the petrophysical relations are valid.

Key words: Electrical resistivity tomography (ERT); Inverse theory; Joint Inversion; Tomography; Seismic tomography.

1 INTRODUCTION

Tomographic techniques based on geophysical measurements are an indispensable tool when detailed subsurface models are required. Models in terms of geophysical parameters, such as seismic velocities or electric resistivities, are often sufficient if only structural information, such as layer boundaries, is of interest. However, if quantitative estimates of geotechnical or petrophysical parameters, such as porosity, permeability or saturation, are required, inversion for these parameters is advantageous, especially if (petrophysical) priors from laboratory measurements or *in-situ* measurements are available.

Inverting for petrophysical quantities is often significantly more difficult than inverting for geophysical models. This is, among other reasons, because petrophysical models are often overparametrized and multiple petrophysical parameters are needed to explain a single geophysical quantity. Although traditional geophysical inversions are also commonly overparametrized, in the sense that the number of model parameters exceeds the number of measurements, the introduction of petrophysical relations with multiple independent parameters further exacerbates this issue. For example, in the Archie equation (G. Archie 1942), which describes pore-fluid-dominated electrical conduction in porous media, resistivity is (traditionally) described by five parameters: porosity, pore–water saturation, pore–water resistivity and the saturation and cementation exponents. In such cases, inversion for all parameters is impossible, since multiple parameter combinations can explain the measured data. Therefore, most parameters are usually estimated once from laboratory or other data sources and then treated as constants throughout the tomography.

By treating most parameters within the petrophysical relation as constants, errors in the estimation of these (constant) parameters cannot be corrected for by the inversion. These errors are then compensated for by the inversion parameter, leading to inaccurate inversion results. Furthermore, using only a single geophysical modality often provides limited resolution. To address this ambiguity and constrain the petrophysical model better, joint inversion techniques that exploit data from multiple geophysical methods are often used.

In recent years, a variety of joint inversion techniques have been investigated, including methods that incorporate petrophysical constraints as additional misfit terms (B. Heincke et al. 2017) or that employ adaptive weighting and inversion schemes (D. Domenzain et al. 2020; T. Qin et al. 2024). However, the two most flexible and widely used approaches to date remain structural and petrophysical coupling. Joint structural inversion (JSI) assumes separate geophysical models of the subsurface. The similarity of the resulting models or tomograms is enforced by aligning the structural features of the model, that is, their edges. Although various methods have recently been proposed to quantify the alignment of structures (see e.g. B. Crestel et al. 2019), cross-gradient coupling, as introduced by L. A. Gallardo & M. A. Meju (2003), remains the most widely used technique in research and has been applied in a wide range of applications.

The application of JSI results in two separate geophysical models. These models can then be transformed into petrophysical models using petrophysical relationships. However, the resulting petrophysical models do not match quantitatively, since the models are only structurally coupled, making a consistent interpretation difficult. In contrast, Joint Petrophysical Inversion (JPI) assumes a single petrophysical model, of which geophysical models for the different methods are derived by petrophysical relationships. Therefore, JPI also couples the models quantitatively and (often) provides a superior and unique quantitatively interpretable tomogram (A. Abubakar et al. 2012).

JPI has been successfully applied in various contexts (e.g. permafrost imaging and hydrocarbon exploration) but requires precise knowledge about the petrophysical relationships in the full model domain. For example, in petrophysical inversions based on Archie's law, it is typically assumed that the cementation exponent, the saturation exponent and the pore-fluid resistivity are well known, and inversion is performed only for saturation and/or porosity. If the parameters of the petrophysical relation are only partially known or fully unknown, these parameters must be included in the inversion itself. Inverting for multiple parameters of the petrophysical laws strongly increases the number of unknowns within the inversion problem and therefore drastically reduces the quality of the resulting tomograms (F. M. Wagner et al. 2019). If, in contrast, the petrophysical laws themselves are invalid, then JPI can often not be applied.

In our contribution, we present an approach to use petrophysical and structural coupling within a common inversion framework, by splitting the model domain into two regions. In regions where the petrophysical relationships hold, the subsurface is described by a common petrophysical model, and the methods are petrophysically coupled. In regions where the petrophysical relations are not valid, the subsurface is described by separate geophysical models for each method, which are merely structurally coupled. We demonstrate the effectiveness of our novel method in a synthetic CO_2-experiment and compare it with pure petrophysical and structural joint inversion.

In addition, we discuss the possibility of automatically detecting regions with invalid petrophysical relationships purely on the basis of the recorded data. For this, standalone inversions are performed based on the separate data. In regions, where both standalone methods suggest similar model updates, the petrophysical relations are assessed to be valid, and the regions remain coupled petrophysically. In regions for which both standalone methods have sufficient data coverage but suggest strongly dissimilar model updates, the petrophysical relations are judged to be invalid, and the models are decoupled. Finally, we include the automatic detection of zones with invalid petrophysical relations and present a partially joint petrophysical inversion scheme that does not rely on prior information about the validity of petrophysical relations.

2 METHODOLOGY

2.1 Partially joint petrophysical inversion

In the following section, we introduce the theoretical framework for a partially decoupled joint petrophysical inversion. Without loss of generality, we will restrict ourselves to two geophysical methods, namely ERT and traveltime seismics (TT). We parametrize the domain with saturation and use Archie's law and a Brie-Gassmann model as petrophysical relations. Archie's Law, linking saturation to electrical resistivities, and the Brie-Gassmann model, mapping saturations into P-wave velocities, will be introduced in detail in Section 3. The framework can be generalized to multiple data sets, as well as different geophysical methods by exchanging model parametrization, petrophysical relations and forward operators.

In conventional JPI (see Fig. 1a), the (discretized) subsurface is modelled by a single saturation model vector $\boldsymbol{m}$, which translates by petrophysical relationships (e.g. Archies law and the Brie-Gassmann model) into separate geophysical model vectors for resistivities $\boldsymbol{\rho}$ and P-wave velocities $\boldsymbol{v_p}$. As described above, we keep all other parameters in these relationships fixed and invert only for saturation, although inversion for multiple parameters is, in principle, possible. For the partially joint petrophysical inversion (P-JPI), we assume that the petrophysical relations only hold in a subdomain of the model, say the first (trusted) T model cells. In the trusted cells, we can parametrize the model using saturations. In the remaining untrusted cells, the petrophysical relations do not hold and so saturation cannot be reliably inferred from velocity or resistivity values. Therefore, the model must be characterized geophysically in terms of resistivities and velocities, respectively. We then describe the subsurface with separate model vectors for each method, with the constraint that the first T model values are equal. The ERT model $\boldsymbol{m^E}$ and the TT model $\boldsymbol{m^S}$ are then parametrized as

$$\boldsymbol{m^E} = \left(m_1, \ldots, m_T, m^E_{T+1}, \ldots, m^E_N\right) \tag{1}$$

$$\boldsymbol{m^S} = \left(m_1, \ldots, m_T, m^S_{T+1}, \ldots, m^S_N\right). \tag{2}$$

Since the first T components of the model vector coincide, we can remove duplicates and combine both model vectors to a joint model vector

$$\boldsymbol{m} = \left(m_1, \ldots, m_T, m^E_{T+1}, \ldots, m^E_N, m^S_{T+1}, \ldots, m^S_N\right). \tag{3}$$

Denoting the petrophysical relations linking saturation to resistivities as p^E, as well as the petrophysical relation linking saturations to P-wave velocities as p^S, the geophysical parameter vectors follow

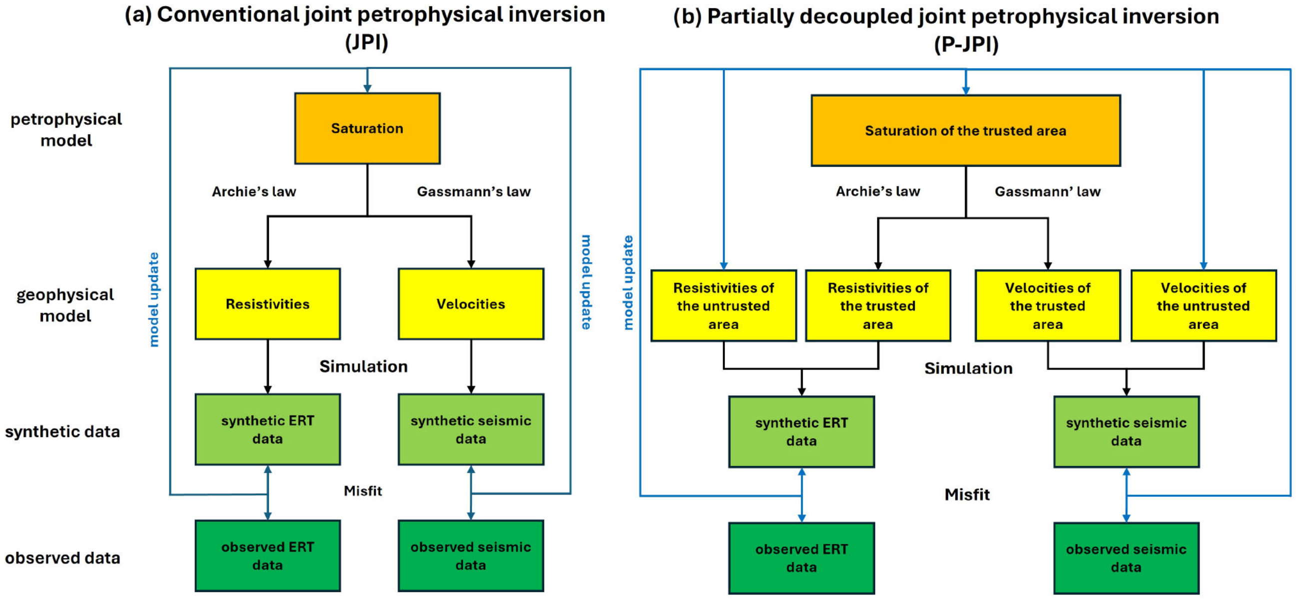

Figure 1. Inversion schemes for conventional (a) and partially decoupled joint petrophysical inversion (b) for two geophysical data sets (ERT and Traveltime seismics).

as

$$\begin{aligned} \boldsymbol{\rho} &= \left(p^E(m_1), \ldots, p^E(m_T), m^E_{T+1}, \ldots, m^E_N\right) \quad \text{and} \\ \boldsymbol{v_p} &= \left(p^S(m_1), \ldots, p^S(m_T), m^S_{T+1}, \ldots, m^S_N\right). \end{aligned} \tag{4}$$

Based on the geophysical model vectors, we can calculate the synthetic response of the models. Given a fixed acquisition scheme, the resistivity model is mapped by the ERT-forward operator into apparent resistivities, which are collected in the synthetic data vector $\boldsymbol{d}^{\boldsymbol{E}}_{\text{syn}}$. Similarly, for given shot and sensor positions, the *P*-wave velocity model is mapped by the traveltime-forward operator to traveltimes, which are collected in the synthetic data vector $\boldsymbol{d}^{\boldsymbol{S}}_{\text{syn}}$.

We aim to minimize data misfit between observed and synthetic data in the least-squares sense. Therefore, we employ a Gauss–Newton scheme and collect the residual vectors of the ERT and TT data

$$\boldsymbol{\Psi}^{\boldsymbol{E}} = \boldsymbol{d}^{\boldsymbol{E}}_{\text{obs}} - \boldsymbol{d}^{\boldsymbol{E}}_{\text{syn}} \quad \text{and} \quad \boldsymbol{\Psi}^{\boldsymbol{S}} = \boldsymbol{d}^{\boldsymbol{S}}_{\text{obs}} - \boldsymbol{d}^{\boldsymbol{S}}_{\text{syn}},$$

and the sensitivity matrices

$$\boldsymbol{J}^E = \frac{\partial \boldsymbol{d}^{\boldsymbol{E}}_{\text{syn}}}{\partial \boldsymbol{m}^E} \quad \text{and} \quad \boldsymbol{J}^S = \frac{\partial \boldsymbol{d}^{\boldsymbol{S}}_{\text{syn}}}{\partial \boldsymbol{m}^S},$$

where the sensitivities of the data with respect to saturation are obtained using the chain rule [see e.g. Appendix A of F. M. Wagner et al. (2019)]. We employ a first-order smoothing, realized by the smoothing matrix $\boldsymbol{R}$, together with a step width damping, realized by the identity matrix $\mathbf{I}$, to steer the convergence behaviour of the inversion. The smoothing of the saturation models for the different data is weighted with weights α^E, α^S, the step width damping with weights β^E, β^S. To avoid smoothing between the coupled and the decoupled regions, we remove rows from the smoothing matrix $\boldsymbol{R}$, which have non-zero components in the first (coupled) T columns, as well as non-zero components in the remaining (uncoupled) columns.

We introduce the following notation to adjust the individual matrices to the joint model vectors: For a matrix $\boldsymbol{A}$, let $\boldsymbol{A_{-T}}$ denote the matrix consisting of the first T columns of $\boldsymbol{A}$ and $\boldsymbol{A_{T-}}$ denote the matrix consisting of the columns from $T+1$ onwards.

We employ a constant weight of one for the ERT data misfit and weigh the seismic traveltime data misfit with a factor of γ. With this, we can set up the full Jacobian matrix $\boldsymbol{J}$, the damping matrix $\boldsymbol{D}$ and the right-hand side vector $\boldsymbol{b}$ as

$$\boldsymbol{J} = \begin{pmatrix} \boldsymbol{J}^{\boldsymbol{E}}_{\boldsymbol{-T}} & \boldsymbol{J}^{\boldsymbol{E}}_{\boldsymbol{T-}} & \boldsymbol{0} \\ \gamma\, \boldsymbol{J}^{\boldsymbol{S}}_{\boldsymbol{-T}} & \boldsymbol{0} & \gamma\, \boldsymbol{J}^{\boldsymbol{S}}_{\boldsymbol{T-}} \end{pmatrix}, \quad \boldsymbol{D} = \begin{pmatrix} \alpha^E \boldsymbol{R_{-T}} & \alpha^E \boldsymbol{R_{T-}} & \boldsymbol{0} \\ \gamma\alpha^S \boldsymbol{R_{-T}} & \boldsymbol{0} & \gamma\alpha^S \boldsymbol{R_{T-}} \\ \beta^E \boldsymbol{I_{-T}} & \beta^E \boldsymbol{I_{T-}} & \boldsymbol{0} \\ \gamma\beta^S \boldsymbol{I_{-T}} & \boldsymbol{0} & \gamma\beta^S \boldsymbol{I_{T-}} \end{pmatrix},$$

$$\boldsymbol{b} = \left(\begin{array}{c} \boldsymbol{\Psi}^{\boldsymbol{E}} \\ \gamma\boldsymbol{\Psi}^{\boldsymbol{S}} \\ \hline -\alpha^E \boldsymbol{R}\boldsymbol{m}^{\boldsymbol{E}} \\ -\gamma\alpha^S \boldsymbol{R}\boldsymbol{m}^{\boldsymbol{S}} \\ \boldsymbol{0} \\ \boldsymbol{0} \end{array}\right). \tag{5}$$

We then apply two variable transformations: First, we apply a logarithmic barrier transformation with the lower barrier b_l and the upper barrier b_u, using different barriers depending on whether the model is described by saturation, resistivities or velocities. With this, we constrain the model values to the interval (b_l, b_u) and exclude unreasonable model values. This is especially important for the petrophysically trusted part of the model to constrain the saturation model to values above zero and below one. We define the parameter transformation $\varphi(x) = \frac{\log(x-b_l)}{\log(b_u-x)}$, set $\tilde{\boldsymbol{m}} = \varphi(\boldsymbol{m})$ and refer to this vector as the model vector in the log-barrier domain. To account for the variable transformation, we adjust the Jacobian and damping matrix according to the product (and inverse function) rule and refer to the transformed matrices as $\tilde{\boldsymbol{J}}$, $\tilde{\boldsymbol{D}}$. For a detailed derivation, we refer the reader to the Appendix A. The minimization problem solved in iteration i then reads as follows:

$$\begin{aligned} &\min_{\tilde{m}} \left(\|\Psi^E\|_2^2 + \alpha^E \|\boldsymbol{R}m_i^E\|^2 + \beta^E \|m_i^E - m_{i-1}^E\|^2\right) \\ &+\gamma \left(\|\Psi^S\|_2^2 + \alpha^S \|\boldsymbol{R}m_i^S\|^2 + \beta^E \|m_i^S - m_{i-1}^S\|^2\right) \quad \text{for } i \geq 1 \end{aligned} \tag{6}$$

Secondly, we introduce a variable scaling, acting as a right preconditioner, to cope with different magnitudes of sensitivities. Let therefore $\boldsymbol{S}$ be the matrix with the inverse of the column sums of

$\tilde{\boldsymbol{J}}$ on the diagonal. We apply the variable transformation to the log-barrier model vector as $\boldsymbol{\mu} = \boldsymbol{S}^{-1}\tilde{\boldsymbol{m}}$. The Gauss–Newton model update is then given as the least-squares solution of the system

$$\begin{pmatrix} \tilde{\boldsymbol{J}}\boldsymbol{S} \\ \hdashline \tilde{\boldsymbol{D}} \end{pmatrix} \Delta\mu = \boldsymbol{b}. \tag{7}$$

The update of the model in the log-barrier domain then follows as

$$\boldsymbol{\Delta\tilde{m}}_i = \boldsymbol{S}\left(\left(\tilde{\boldsymbol{J}}S\right)\tilde{\boldsymbol{J}}S + \boldsymbol{D^2}\right)^{-1}(\boldsymbol{JS})^{S}\,\boldsymbol{b} \text{ for } i = 1, 2, \ldots. \tag{8}$$

Both the full Jacobian matrix and the individual matrices comprising the Jacobian in eq. (5) are usually sparse, so iterative solvers for the solution of eq. (7) are highly recommended. Lastly, we apply an absolute lower limit Δ_l and an upper limit Δ_u to updates of the models during a single step, to avoid excessive model updates. Again, these absolute limits are chosen independently for the model values in terms of saturation, resistivities and velocities. The update of the petrophysical model is then given as

$$\begin{aligned} \boldsymbol{m}_{i+1} &= \boldsymbol{m}_i + \boldsymbol{\Delta m}_i \text{ with } \boldsymbol{\Delta m}_i \\ &= \min\left(\Delta_u, \max\left(\Delta_l, \varphi^{-1}\left(\tilde{\boldsymbol{m}}_i + \boldsymbol{\Delta\tilde{m}}_i\right) - \boldsymbol{m}_i\right)\right) \text{ for } i = 1, 2, \ldots. \end{aligned}$$

In Fig. 1 we show a schematic overview of the conventional joint petrophysical inversion and the partially decoupled joint petrophysical inversion. From this overview, it is evident that the JPI-scheme is a specialization of the P-JPI-scheme: If we trust the petrophysical relationship throughout the full domain, we have $T = N$. Then columns two and three of $\boldsymbol{J}$ and $\boldsymbol{D}$ are empty and the P-JPI scheme becomes the JPI scheme. In this case, the smoothing and damping constraints in matrix $\boldsymbol{D}$ are duplicates and can be simplified. In a similar fashion, a classical single-data petrophysical inversion scheme can be derived from the JPI scheme, if one of the data sets (i.e. its corresponding rows in $\boldsymbol{J}$ and $\boldsymbol{D}$) is removed from the Gauss–Newton system.

2.2 Partially structurally joint petrophysical inversion

Within the P-JPI scheme, the model domain is fully coupled (within the first T model cells) or completely independent (within the remaining model cells). However, also within the independent parts of the domain, the models are likely to share structural similarities, even if the petrophysical relations in these regions are faulty. Therefore, it is obvious to relax the petrophysical coupling to a mere structural coupling, instead of completely decoupling the models.

In this work, we implement structural coupling using cross-gradient terms. For a discretized model, the cross-gradient terms aim to minimize the cross product between the spatial gradients of the models, so that the minimization problem is augmented with the following term

$$\sum_{i=1}^{N} \|\nabla\boldsymbol{\rho}(i) \times \nabla\boldsymbol{v}_p(i)\|^2.$$

In the case of a 2-D model domain, each cross-product reduces to a single component, whereas for a 3-D model domain each summand can be substituted by its three components. The cross-gradient term then constitute an additional set of equations and enters the Gauss–Newton system as additional rows with a corresponding weight δ and right-hand site

$$\boldsymbol{b}_X = \left(\nabla\boldsymbol{\rho}(1) \times \nabla\boldsymbol{v}_p(1), \ldots, \nabla\boldsymbol{\rho}(N) \times \nabla\boldsymbol{v}_p(N)\right).$$

The sensitivities of the cross-gradient term with respect to the discrete model require discretizing the spatial gradient operator. This is usually done either with an appropriate finite difference scheme if the domain is modelled by a structured grid (L. A. Gallardo & M. A. Meju 2003), or by a Taylor expansion if the domain is modelled by an unstructured grid (C. Jordi et al. 2020). As a result of the discretization, the gradient in each model cell depends linearly on the model value of the cell itself and its neighbours. With that, the sensitivities of the cross-gradient term with respect to the model vector $\boldsymbol{m}$ can be calculated and stored in the sensitivity matrix $\boldsymbol{X}$. For a thorough derivation of the sensitivities, we refer the reader to Appendix B.

The cross-gradient matrix $\boldsymbol{X}$ is now adjusted according to the parameter transformations, as described in Section 2.1, resulting in the adjusted matrix $\tilde{\boldsymbol{X}}$. With a given weight of δ for the cross-gradient constraints, the model update for the PS-JPI is then given as the least-squares solution of the system

$$\begin{pmatrix} \tilde{\boldsymbol{J}}\boldsymbol{S} \\ \tilde{\boldsymbol{D}} \\ \hdashline \delta\tilde{\boldsymbol{X}} \end{pmatrix} \Delta\mu = \begin{pmatrix} \boldsymbol{b} \\ \hdashline -\delta\boldsymbol{b}_X \end{pmatrix}. \tag{9}$$

2.3 Joint structural inversion

In the previous section we added structural coupling to the domain, where the models are not petrophysically coupled. We can obtain the classical JSI scheme by considering a domain without any petrophysical coupling. Therefore, the PS-JPI scheme can be viewed as a joint generalization of the JPI scheme and the JSI scheme: If we trust the petrophysical relationships over the entire model domain, the model is characterized by a single petrophysical model. With this, columns two and three of $\boldsymbol{J}$ and $\boldsymbol{D}$ disappear together with the cross-gradient terms, and we obtain a classical JPI scheme. In contrast, if we do not trust the petrophysical relationship anywhere in the model domain, the subsurface is characterized by two separate geophysical model vectors. Therefore, the first column of $\boldsymbol{J}$ and $\boldsymbol{D}$ vanishes, the cross-gradient terms act on the entire model domain, and we obtain a classical JSI scheme.

3 SYNTHETIC EXAMPLES

The P-JPI algorithm is designed to enable a partially joint petrophysical inversion in the case where the governing petrophysical laws are only valid in parts of the domain. Therefore, in the first section of the chapter, we introduce a synthetic case study, which is based on a real CO_2-injection experiment. In the second section, we show that neither petrophysical inversions based on a single data set (‘standalone’ inversions) nor a conventional JPI approach can explain the recorded data. Finally, in the last section we show the application of the P-JPI to the synthetic data set and compare it to its conventional alternatives in single-data inversions and geophysical JSI.

3.1 Synthetic model and data

For our synthetic study, we consider a 2-D tomography experiment, using ERT and seismic traveltime data, to image the CO_2 saturation S_{CO_2} for a Carbon Capture and Storage (CCS) application. We use a model consisting of two regions, the CO_2-reservoir and its caprock, which are separated by a straight, diagonal, lithological boundary. Two boreholes with a separation of 50 m have been drilled into the reservoir. Through these boreholes CO_2 has been injected into the reservoir, which was then trapped at the boundary with the caprock,

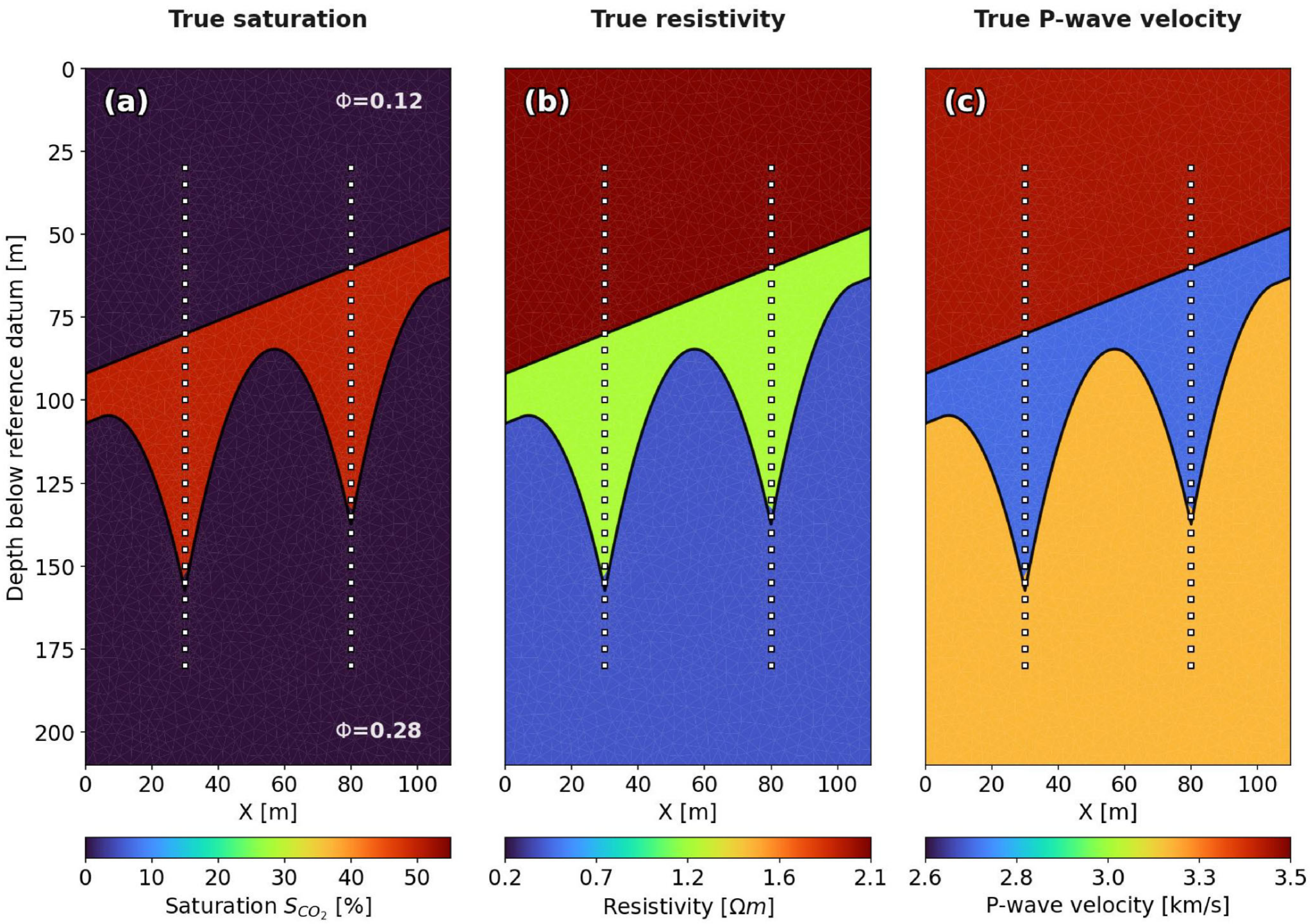

Figure 2. Geometry and ground-truth saturation S_{CO_2} (a), resistivity ρ (b), and P-wave velocity v_p (c) parametrization of the synthetic model. Sensor positions are indicated by white squares. The outline of the CO_2-plume is highlighted by a black line.

forming a distinct flag-shaped plume. The geometry is shown in the ground-truth saturation model in Fig. 2(a).

Within the reservoir, we assume complete knowledge of the governing petrophysical laws. We assume that the reservoir consists of porous rock, for example sandstone. The porespace is fully saturated with pore water, CO_2 or a mixture thereof. That is, for the water saturation S_W, the CO_2 saturation follows as $S_{\mathrm{CO}_2} = 1 - S_W$. In contrast, the caprock consists of an impermeable rock, for example shales or clay-rich minerals, in which the petrophysical laws of the reservoir are not valid.

For the reservoir, we employ Archie's law (G. Archie 1942) to model the relation between CO_2 saturations and resistivities. By assuming a fully saturated porespace, Archie's equation can be stated in terms of the CO_2 saturation as

$$\rho = \rho_W \phi^{-m} \underbrace{(1 - S_{\mathrm{CO}_2})}_{S_W}{}^{-n} \tag{10}$$

for porosity ϕ, pore water resistivity ρ_W, cementation exponent m and saturation exponent n.

For the relation between P-wave velocities and CO_2 saturations, we use Gassmann's fluid substitution model (F. Gassmann 1951) together with a Brie model (A. Brie et al. 1995) to describe the elastic properties of the fluid mixture. Generally, the P-wave velocity follows from the shear modulus μ, which is not affected by the fluid in the pore space, the effective bulk modulus K_{eff} and effective density ϱ_{eff} of the rock by the constitutive equation

$$v_p = \sqrt{\varrho_{\mathrm{eff}}^{-1}\left(K_{\mathrm{eff}} + \frac{4}{3}\mu\right)}. \tag{11}$$

The effective density of the rock is given as the arithmetic mean of the density of the rock matrix $\varrho_{\mathrm{matrix}}$ and the density of the pore fluid ϱ_{fluid}, where the mean is taken with respect to the porosity ϕ. The density of the pore fluid is itself given as the arithmetic mean (with respect to the saturation S_{CO_2}) of the density of the pore water ϱ_{water} and the density of the CO_2, ϱ_{CO_2}, as

$$\begin{aligned}\varrho_{\mathrm{eff}} &= (1-\phi)\varrho_{\mathrm{matrix}} + \phi\varrho_{\mathrm{fluid}} \text{ and } \varrho_{\mathrm{fluid}} \\ &= S_{\mathrm{CO}_2}\varrho_{\mathrm{CO}_2} + (1 - S_{\mathrm{CO}_2})\varrho_{\mathrm{water}}.\end{aligned} \tag{12}$$

The effective bulk modulus K_{eff} of the fluid filled rock is given by Gassmann's equation

$$\begin{aligned}K_{\mathrm{eff}} &= \frac{L}{1+L} K_{\mathrm{matrix}} \text{ with} \\ L &= \frac{K_{\mathrm{dry}}}{K_{\mathrm{matrix}} - K_{\mathrm{dry}}} + \frac{K_{\mathrm{fluid}}}{\phi\,(K_{\mathrm{matrix}} - K_{\mathrm{fluid}})},\end{aligned} \tag{13}$$

where K_{matrix} is the bulk modulus of the rock matrix, K_{dry} is the dry rock bulk modulus and K_{fluid} is the fluid bulk modulus. The bulk modulus of the fluid, which is a mixture of pore water and CO_2, is

Table 1. Elastic parameters used in the Brie-Gassmann model. The values are taken from A. Ivanova et al. (2012) or chosen so that the maximum and minimum seismic velocities reported in A. Ivanova et al. (2012) are reproduced.

	K/μ (GP$_a$)		ϱ (kg m^{-3})		v (m s^{-1})
K_{CO_2}	0.01	ϱ_{CO_2}	231.53	$v_{p,\text{ketzin}}^{\min}$	~ 2720
K_{water}	3.63	ϱ_{water}	1164.59	$v_{p,\text{ketzin}}^{\max}$	~ 3200
K_{matrix}	37.78	ϱ_{matrix}	2670.89	–	–
K_{dry}	3.5	–	–	–	–
μ	8.1	–	–	–	–

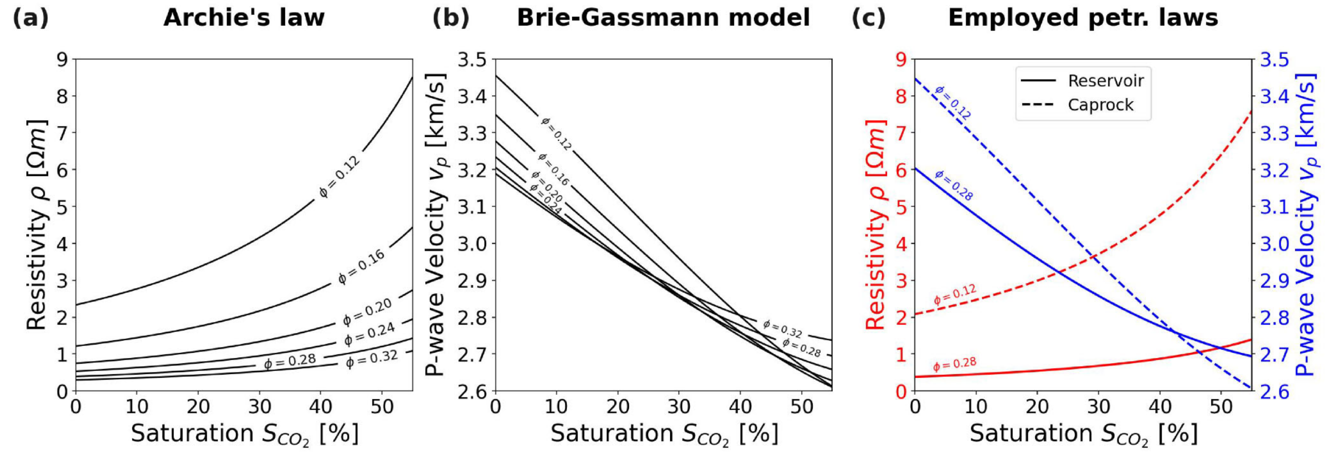

Figure 3. Modelled petrophysical relations mapping saturation S_{CO_2} to resistivity ρ (a), and P-wave velocity v_p (b) for different porosity parameters. The petrophysical relationships employed for caprock and reservoir are shown in (c).

modelled by Brie's equation (with exponent 3) as

$$K_{\text{fluid}} = (K_{\text{water}} - K_{CO_2})\underbrace{(1 - S_{CO_2})}_{S_W}{}^3 + K_{CO_2}. \tag{14}$$

To parametrize the model, we follow reports from the Ketzin CO_2 storage project, which was established around 2004 by the GFZ Helmholtz Centre for Geosciences close to Berlin (Germany). During this project, CO_2 was injected into a sandstone formation at 650 m depth, which is overburdened by a approximately 210 m thick multibarrier caprock system (A. Förster et al. 2006), and was monitored through surface measurements and four deep boreholes. During their petrophysical laboratory experiments, A. Ivanova et al. (2012) reported maximum CO_2 saturations of about 50 per cent. Therefore, we parametrize the ground-truth model with CO_2 saturations of 50 per cent within the CO_2 plume and 0 per cent within the caprock and the remainder of the reservoir. The ground-truth saturation model is shown in Fig. 2(a).

For the Brie-Gassmann model, we use the elastic moduli reported in A. Ivanova et al. (2012) for sample B2-3b. Unfortunately, the authors do not provide values for μ and K_{dry}, so we have to choose appropriate values. The elastic moduli used and the velocities reported by A. Ivanova et al. (2012) are summarized in Table 1.

For the parametrization of Archie's law, we use a saturation exponent of $n = 1.62$ as reported in J. Kummerow & E. Spangenberg (2011) for sample B2-3b together with a typical cementation exponent for sandstone of $m = 2$. We then choose the pore fluid resistivity as $\rho_W = 0.03$, so that we get resistivity values between $0.38\ \mu$m for 0 per cent CO_2-saturation and $1.18\ \mu$m for 50 per cent CO_2-saturation, which are close to the values reported in J. Kummerow & E. Spangenberg (2011).

In Figs 3(a) and (b), we show the derived petrophysical laws within the relevant saturation range for varying values of porosity ϕ. It is noteworthy that Archie's law is very sensitive to changes in porosity, that is, a small error in the estimate of porosity leads to significant errors in the estimate of the CO_2 saturation. This effect can be observed in Fig. 3(a), where the curves corresponding to different porosities become almost flat for small resistivity values. Therefore, small changes in resistivity amount to large changes in the estimated saturation, which makes precise knowledge of the porosity imperative.

In contrast, the P-wave velocity is less sensitive to changes in porosity, as shown in Fig. 3(b), where the curves corresponding to different porosities are less flat. Furthermore, the saturation-P-wave velocity diagram exhibits several intersections between curves for different porosities. This implies that the same P-wave velocity can be explained by different porosity values for the same saturation value, highlighting the inherent ambiguity between saturation and porosity for seismic data.

For our synthetic model, we assume a porosity of $\phi = 0.28$ within the reservoir layer, as reported by J. Kummerow & E. Spangenberg (2011) for the B2-3b sample. Within the caprock layer, the petrophysical relations described above do not hold, but for simplicity we derive geophysical parameters, as if the caprock were subject to the same petrophysical laws and a porosity of $\phi = 0.12$, as has been reported for the caprock in the Ketzin project (B. Norden et al. 2010). The petrophysical relations used for the reservoir and the caprock are also shown separately in Fig. 3(c).

From the true saturation model and the different petrophysical relations for the caprock and the reservoir, the ground-truth geophysical models for the resistivities and P-wave velocities can be derived. The geophysical ground-truth models are shown in Figs 2(b) and (c), where we plot the depth according to a reference datum at ~550 m below subsurface. The CO_2 plume is characterized by high resistivities, caused by the displacement of conductive pore water, and low P-wave velocities, due to the small bulk modulus of CO_2,

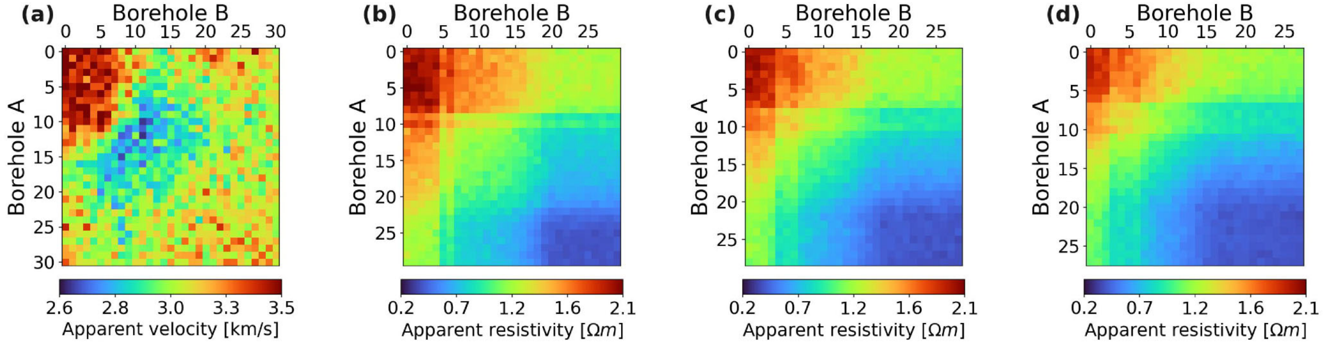

Figure 4. Observed data shown in cross-plots, with sensors indexed from top to bottom of the borehole. In panel (a) we show the observed apparent velocities. In panels (b) to (d) the observed apparent resistivities for fixed injection/measurement electrode distance of 1 sensor or 5 m (b), 2 sensors or 10 m (c) and 3 sensors or 15 m are shown.

compared to the remainder of the reservoir. Within the caprock, the low porosity leads to high resistivity values, which are significantly higher than those from the CO_2-plume, together with high values of *P*-wave velocities.

To image the CO_2-plume, the boreholes are equipped with co-located ERT and seismic sensors, of which we use the traveltime data. Each borehole has a total of 31 sensors with a 5 m spacing, covering the depth interval between 30 and 180 m. For the ERT measurements, we consider configurations in which current is injected across both boreholes. Both potential measurement electrodes are located either 5, 10 or 15 m above or below the injection electrodes. The measurement configurations used are shown in Fig. C1. For the seismic traveltime measurements, we only consider the data, where sources are placed in the left borehole (A) with receivers placed in the right borehole (B).

For the simulation of the synthetic data and the calculation of the geophysical sensitivities, we use the open-source library pyGIMLi (C. Rücker et al. 2017). The ERT simulation is based on the finite element scheme for the Poission’s equation (C. Rücker et al. 2006) and the traveltime seismic simulations are based on Djikstras algorithm (T. J. Moser 1991). For the forward simulations, we use a refined version of the coarse inversion mesh. Additionally, we choose to add the layer boundary between the caprock and the reservoir to the meshes, since we assume that the location is known from the logging data, and omit smoothing over the layer boundary. Both the forward and the inverse mesh are augmented with a 20 m thick boundary mesh to mitigate boundary effects. The boundary mesh is omitted from the visualizations for visual clarity.

We simulate the response of the geophysical ground-truth models, which are shown in Figs 2(b) and (c), and pollute both data sets with 3 per cent relative Gaussian noise. From the observed noisy seismic data, we then calculate apparent velocities and display them in a cross-plot in Fig. 4(a). For the ERT data, we divide the configurations into six subsets, where the measurement electrodes have a fixed offset of 1, 2 or 3 sensor positions (respectively, 5, 10 or 15 m) above or below the injection electrodes. We omit the data with measurement electrodes located above the injection electrodes because of reciprocity. The remaining data are shown in separate cross-plots in Figs 4(b) to (d), where the configurations are labelled based on the position of the injection electrodes in the respective boreholes.

The low velocities and high resistivities of the CO_2 plume, as well as the high resistivities and velocities of the caprock, are prominently shown in the data. The TT seismic and ERT data show a remarkably sharp boundary for a rectangle marked by electrode/sensor position 11 in borehole A and electrode/sensor position 7 in borehole B, which are precisely located on the boundary between the caprock and the reservoir. This rectangle corresponds to data that are mainly sensitive to the model parameters of the caprock. Thus, we will use these electrode positions later to quantify the error of the data with respect to the caprock and the reservoir.

3.2 Conventional (joint) petrophysical inversion

Within this section, we first apply a conventional petrophysical inversion to the separate data sets (‘standalone’ inversion) to investigate the resolution capabilities of the individual methods and determine suitable regularization parameters. Using these parameters, we then apply a conventional joint petrophysical inversion and show that, in regions with invalid petrophysical laws, the JPI tomogram strongly depends on the weighting of both data sets and comprises a structured misfit.

For assessing the recovery of the observed data by the inverted model, we use the χ^2 values for the different data, which constitute an average error-weighted least-squares misfit. The χ^2 values for the ERT and seismic traveltime data are defined as

$$\chi_E^2 := \frac{1}{M}\sum_{i=1}^{M}\left(\frac{(\mathbf{d}^{\mathbf{E}}_{\mathbf{obs}} - \mathbf{d}^{\mathbf{E}}_{\mathbf{syn}})(i)}{e^E(i)}\right)^2 \quad \text{and}$$

$$\chi_S^2 := \frac{1}{N}\sum_{i=1}^{N}\left(\frac{(\mathbf{d}^{\mathbf{S}}_{\mathbf{obs}} - \mathbf{d}^{\mathbf{S}}_{\mathbf{syn}})(i)}{e^S(i)}\right)^2, \tag{15}$$

where e^S and e^E are error estimators for the seismic traveltime and ERT data, respectively, and M and N are the number of data points recorded in the corresponding surveys. For this survey, error estimates are given as the standard deviation of the Gaussian distribution used to generate the noise. The χ^2 values can also be used to assess the recovery of the model in specific parts of the model domain. For this, only data sensitive to the specific region under investigation are considered in the sum in eq. (15).

Individual inversions are terminated whenever the model update does not significantly improve the data fit or a maximum number of 35 iterations is reached. Therefore, we terminate the inversion based on the individual data, once a model update leads to a decrease of the corresponding χ^2 value by less than one percent. Consequently, we terminate a joint inversion if the model updates cause both data misfits χ_E^2 and χ_S^2 to decrease by less than one percent.

For the joint inversions, we employ a constant weight of 1 for the ERT data misfit and weigh the seismic data relative to the absolute data sizes by setting $\gamma = \tilde{\gamma}\frac{\|\boldsymbol{d}^{\boldsymbol{E}}_{\text{obs}}\|}{\|\boldsymbol{d}^{\boldsymbol{S}}_{\text{obs}}\|}$, with the TT-weight $\tilde{\gamma}$. For all inversions, we constrain saturations to values between 0 per cent and 55 per cent, resistivities to values between 0.3 and 2.3 Ωm, and *P*-wave velocities to values between 2660 and 3500 $\mathrm{m\,s^{-1}}$.

In Fig. 5 we show the resulting saturation (a to c), resistivity (d, e) and velocity tomograms (f, g) together with the ground truth models for the standalone petrophysical inversions. Within the reservoir, the standalone ERT inversion provides a good recovery of the CO_2-saturations, but the structure of the CO_2-plume appears to be smeared, as the model features significant CO_2-saturation values below the CO_2-plume and outside the monitoring boreholes. In contrast, the standalone TT seismic inversion recovers a sharper boundary of the CO_2-plume, as the transition between high and low saturation values aligns more closely with the true plume boundary, but fails to provide a good quantitative estimate of the CO_2-saturations within the plume.

Within the caprock, neither of the two methods is able to recover the geophysical ground truth model, due to the incorrect petrophysical laws employed (see Fig. 3). In order to match the high resistivities of the ground truth resistivity model, the standalone ERT inversion recovers very high saturation values, which are constrained by the log-barrier at ∼55 per cent. However, the recovered resistivities are still significantly too small. In contrast to that, the standalone TT seismic inversion recovers very small saturation values, in order to match the high velocities of the caprock. In this case, saturations are constrained by the log-barrier at ∼0 per cent and the recovered velocities of ∼3200 $\mathrm{m\,s^{-1}}$ are significantly below the ground truth model, which features velocities of ∼3400 $\mathrm{m\,s^{-1}}$ within the caprock.

Furthermore, both methods exhibit strongly different sensitivity patterns. Whereas the traveltime seismic data are only sensitive to saturation/velocity variations between both boreholes, the ERT data are also sensitive to saturation/resistivity variations up to 25 m outside the monitoring boreholes.

In Fig. 6 we show the data misfit for the recovered models of the standalone ERT and seismic traveltime inversions. The seismic traveltime misfit is significantly smaller compared to the ERT data misfit, indicating lower sensitivity of the seismic data with respect to the CO_2 saturation. Both methods achieve a good data fit for the data points in the bottom right quadrant of the misfit plot, which correspond to data mainly sensitive to the reservoir. Specifically, the TT seismic exhibits an almost perfect χ^2 value close to unity.

In contrast, both methods show a high, strongly structured misfit in the top left quadrant, caused by resistivity and velocity models that deviate significantly from the ground truth. The off-diagonal quadrants, which correspond to mixed sensor configurations between caprock and the reservoir, show low misfit values for the seismic data, but large values for the ERT data. These large misfit values for the ERT indicate that the ERT is unable to compensate for the faulty caprock model, whereas the TT seismic again appears to be more robust.

In summary, standalone inversions of the seismic and ERT data cannot match the observed data when the petrophysical laws are not valid over the entire domain. In the regions where the petrophysical laws apply, the saturation models are mostly recovered accurately, and artefacts are mainly limited to the caprock area. Within the caprock, the correct resistivities and velocities cannot be described by saturations, as they lie outside the parameter range that can be represented by saturations (cf. Fig. 3c). However, if the petrophysical relations are incorrect but the relevant geophysical parameters can be represented by petrophysical parameters (i.e. if the incorrect petrophysical relation covers a smaller geophysical parameter range than the true/used relation), standalone inversions can explain the observed data, but with incorrect saturation estimates.

In the next step, we apply a conventional JPI algorithm to the observed data. In Fig. 7, we show the resulting saturation (a to d), resistivity (e to h) and *P*-wave velocity tomograms (i to l) together with the ground-trust models for TT-weights of 0.1, 1 and 10.

All tomograms show good quantitative recovery of saturations, resistivities and velocities within the lower parts of the reservoir, as well as good recovery of the structure of the CO_2 plume. A strong weight on the ERT data smears the lower boundary of the recovered structure, whereas a strong weight on the seismic data results in a sharper and more accurate recovery of the lower boundary of the CO_2 plume (cf. 7c). However, for strong weights on the seismic data, low-saturation artefacts are introduced in the centre of the CO_2-plume, effectively cutting the plume in half.

In contrast to the reservoir, the resulting tomograms show strong variations in the caprock with the data weighting used. A small TT-weight, and hence a strong relative weight on the ERT data, leads to the recovery of high saturation, and therefore high resistivity values in the caprock, which get constrained by the upper saturation barrier. Again, the resistivities recovered are significantly lower than the ground truth resistivity values in the caprock. The resulting tomograms are comparable to the standalone ERT inversion, which can be seen as a limit case for the TT-weight approaching 0. However, the high saturation values imply that the velocity model is not accurately recovered within the caprock.

In contrast, a large TT-weight, and hence a strong relative weight on the seismic data, leads to the recovery of low saturation and hence high velocity values in the caprock in between both monitoring boreholes, which get constrained by the lower saturation barrier. Again, similarly to the standalone seismic TT inversion, the recovered velocities in the caprock are significantly smaller than the ground truth velocity values in the caprock. Since the traveltime data are only sensitive to the model parameters between the boreholes, high saturation compensation artefacts are introduced by the ERT outside the boreholes, to remedy the inaccurate resistivity model between the boreholes. In this case, the resulting tomograms between the boreholes can again be regarded as a limit case for the TT-weight infinity for all areas which are resolved by both methods.

In summary, the conventional JPI approach cannot match the observed data when the petrophysical laws are not valid within the full domain. In the regions where the petrophysical laws hold, the saturation model is mostly accurately recovered and artefacts are mainly limited to the caprock area. The tomograms from the petrophysical inversions based on the individual data showed that neither the correct resistivities nor velocities can be described with a saturation model. Furthermore, the application of the classical JPI scheme revealed that the different data sets require different saturation models within the caprock to match the data: the ERT data require high saturation to match the high resistivity, whereas the seismic data ask for low saturation to match the high seismic velocities. Therefore, either velocities or resistivities are preferentially recovered based on the chosen data weight, driving the saturation to its corresponding values.

3.3 Partially joint petrophysical inversion

When an accurate petrophysical law is not available, a conventional JPI becomes infeasible, and the coupling has to be either

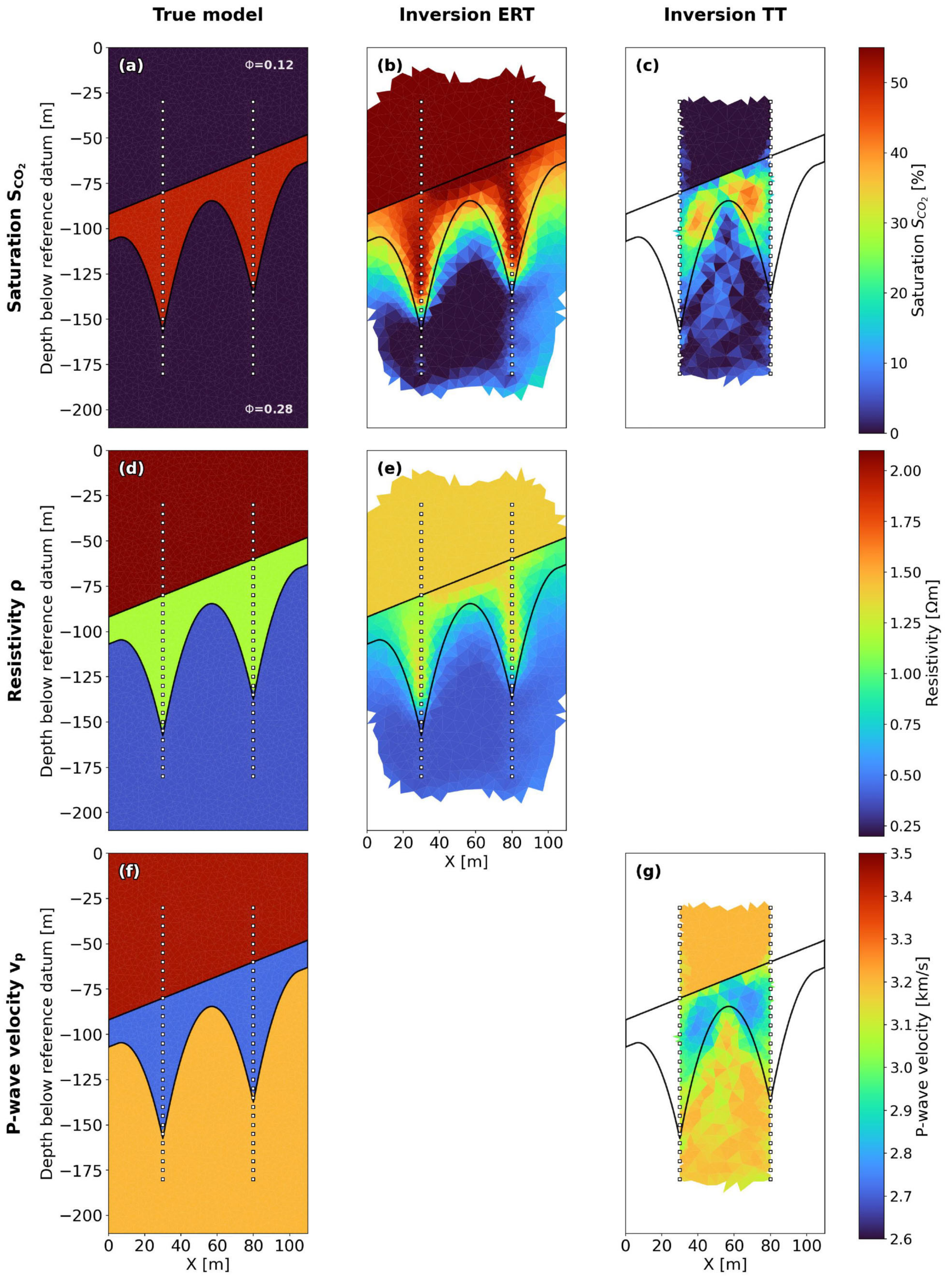

Figure 5. True model parametrizations and corresponding tomograms from the individual petrophysical inversions. Rows display saturation S_{CO_2}, resistivity ρ, and P-wave velocity v_p. Columns show the true models and final tomograms from the ERT and TT seismic inversion. Sensor positions are indicated by white squares. The outline of the CO_2-plume is highlighted by a black line. Cells not resolved by the respective method are shown in white.

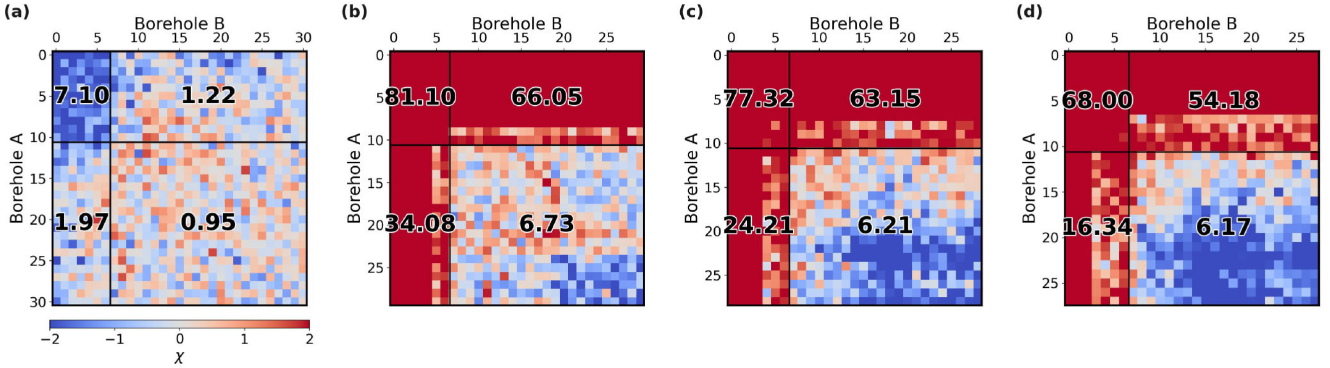

Figure 6. Pointwise data residual for the individual petrophysical inversions shown in cross-plots in multiples of the standard deviation of the added Gaussian noise. Sensors are indexed from top to bottom of the borehole. Panel (a) shows the data residuals of the traveltime data. Panels (b) to (d) show the data residuals of the ERT data for fix injection/measurement electrode distance of 1 sensor or 5 m (b), 2 sensors or 10 m (c) and 3 sensors or 15 m (d). The cross-plots have been subdivided in four 'quadrants' according to the sensitivity of the data to the layer interface and individual χ^2-values have been calculated for each of the quadrants.

relaxed to a structural coupling or completely omitted. Therefore, we apply the P-JPI to the synthetic data and compare the results to the only structurally coupled JSI, and the results of the standalone geophysical inversions. In Fig. 8, we show the ground-truth resistivities and the P-wave velocities (a and e) together with the tomograms of the standalone geophysical inversions (b and f), the tomograms of the JSI (c and g) and the tomograms of the P-JPI (d and h).

The inversions based on the individual data result in different tomograms, which are similar in nature to the standalone petrophysical tomograms shown in Fig. 5, but are able to recover accurate geophysical models within the caprock as well. The tomogram based on the ERT data shows a good recovery of the resistivities for the caprock and reservoir, even outside the boreholes. The resistivity values within the CO_2 plume are well recovered, but the structure remains smeared. In contrast, the tomogram based on seismic traveltimes recovers the structure of the CO_2 plume better, but does not provide a good quantitative recovery of the velocities for the CO_2 plume.

The joint structural inversion provides improved tomograms over the standalone inversions. The ERT tomogram appears mostly unchanged compared to the standalone ERT inversion, with minor improvements in the shape of the CO_2 plume. In contrast, the shape of the CO_2 plume in the TT seismic tomogram is aligned with the ERT tomogram, showing an arc-like outline.

The tomograms provided by the P-JPI constitute a strongly improved model for the reservoir compared to the individual data tomograms and JSI tomograms. The structure of the CO_2 plume is almost perfectly recovered for both the resistivity and the P-wave velocity model. Furthermore, the recovery of the CO_2 plume outside the crosshole setup is significantly improved as a side effect of a more accurate model recovery within the borehole setup.

In Fig. 9, we show the misfit cross-plots for the standalone geophysical inversions, the JSI and the P-JPI. JSI and P-JPI exhibit notably lower misfit values compared to standalone geophysical inversions especially for the large offset ERT data, demonstrating the effectiveness of joint-inversion techniques for this application. The misfits of the P-JPI method are superior to those of the JSI, especially for the seismic TT data and the off-diagonal quadrants of the ERT data.

For the upper left quadrant, all methods exhibit slightly increased misfit levels for the TT data, with the P-JPI method again performing best. For the ERT data, the upper left quadrant does not exhibit increased levels of misfit, which also appears to be randomly distributed. This indicates that the decoupling of the caprock models in fact leads to an accurate data fit.

Furthermore, the lower right quadrants of the ERT misfit exhibit strongly reduced values when compared to the misfit cross-plots of the standalone petrophysical inversions in Fig. 6. Therefore, decoupling the caprock models drastically improves the data fit, even for data that are sensitive mainly to the reservoir model. This again implies that the wrong caprock model trades off with the reservoir and cannot be neglected.

In contrast to the P-JPI, the geophysical standalone inversions as well as the JSI only provide a geophysical model of the domain. These geophysical models can be interpreted as saturation only if their values lie within the range of resistivities or velocities attainable through the petrophysical relationship (cf. Fig. 3c). Specifically, resistivities between 0.38 and 1.4 Ωm and P-wave velocities between 2690 and 3200 $\mathrm{m\,s^{-1}}$ correspond to saturations between 0 per cent and 55 per cent.

In Fig. 10 we show the ground truth saturation model, together with saturation models derived from the standalone geophysical inversions, the JSI and the P-JPI. For most methods, the geophysical parameters of the caprock cannot be interpreted as saturations, since both resistivity and velocity significantly exceed the parameter range that can be associated with saturation by means of the petrophysical relation.

The reservoir saturation models derived from the standalone inversions and the JSI show similar characteristics: For both methods, the ERT provides a smeared but quantitatively good recovery of the saturation within the CO_2 plume. For the JSI, both tomograms show an improved shape of the recovered CO_2 plume, with coherent boundaries. However, large parts of the reservoir region of the ERT tomogram cannot be interpreted as saturations because the recovered resistivities are too small.

In contrast, most parts of the reservoir can be interpreted in terms of saturation for the tomograms derived from the seismic traveltime data. The saturation tomograms for both the standalone and the JSI show a decent recovery of the CO_2 plume shape. The outline of the CO_2 plume of the JSI is aligned with the ERT model. However, both saturation tomograms derived from velocity models show a poor quantitative recovery of the saturation, which is significantly underestimated.

The P-JPI provides an excellent tomographic result for the reservoir saturation model between the boreholes and a good saturation

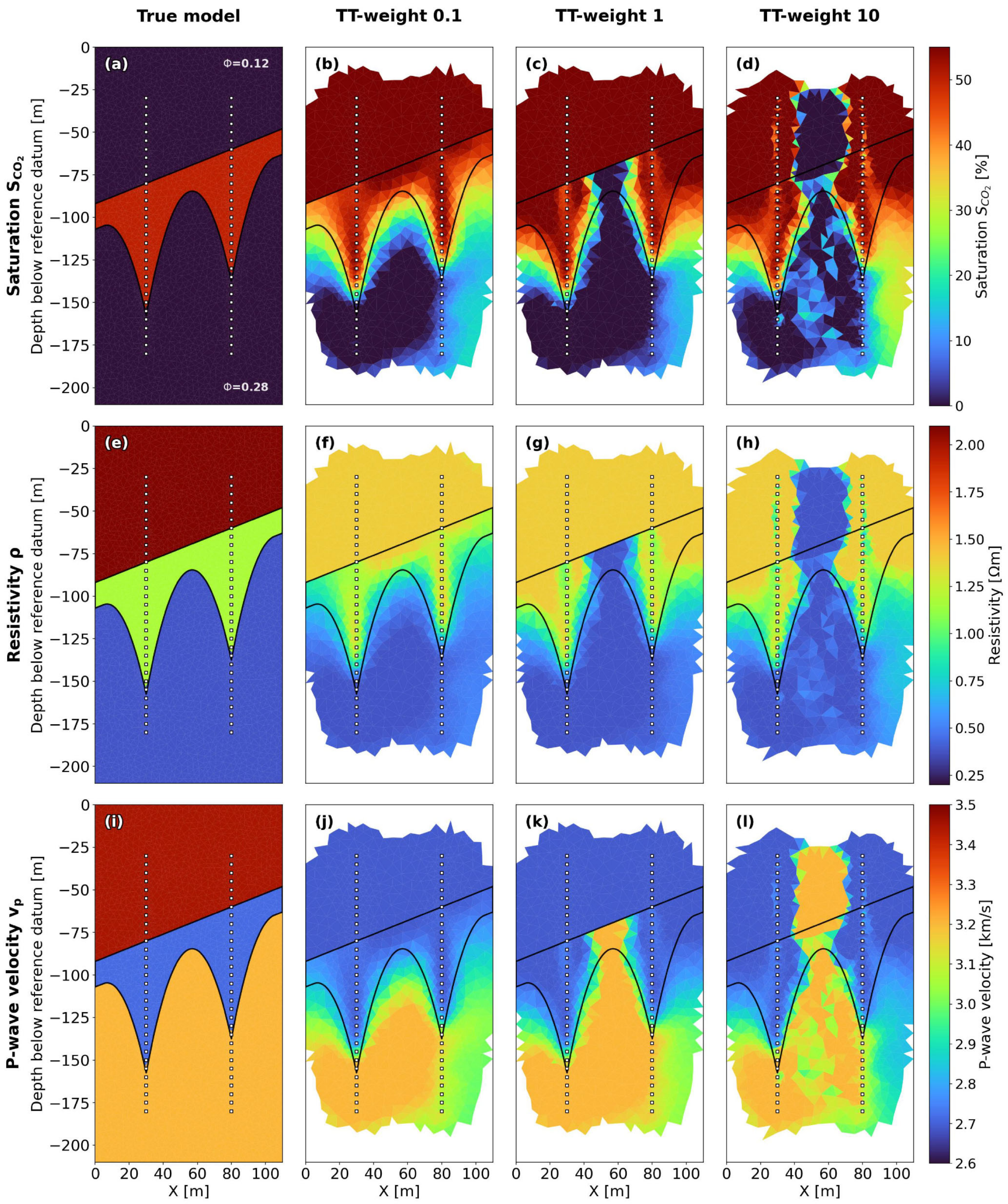

Figure 7. True model parametrizations together and corresponding tomograms from the JPI using different data weighing factors. Rows show saturation S_{CO_2}, resistivity ρ and P-wave velocity v_p. Columns show the true models, and tomograms for data weighing factors of 0.1, 2 and 10, respectively. Sensor positions are indicated by white squares. The outline of the CO_2-plume is highlighted by a black line. Cells not resolved by either ERT or TT seismics are shown in white.

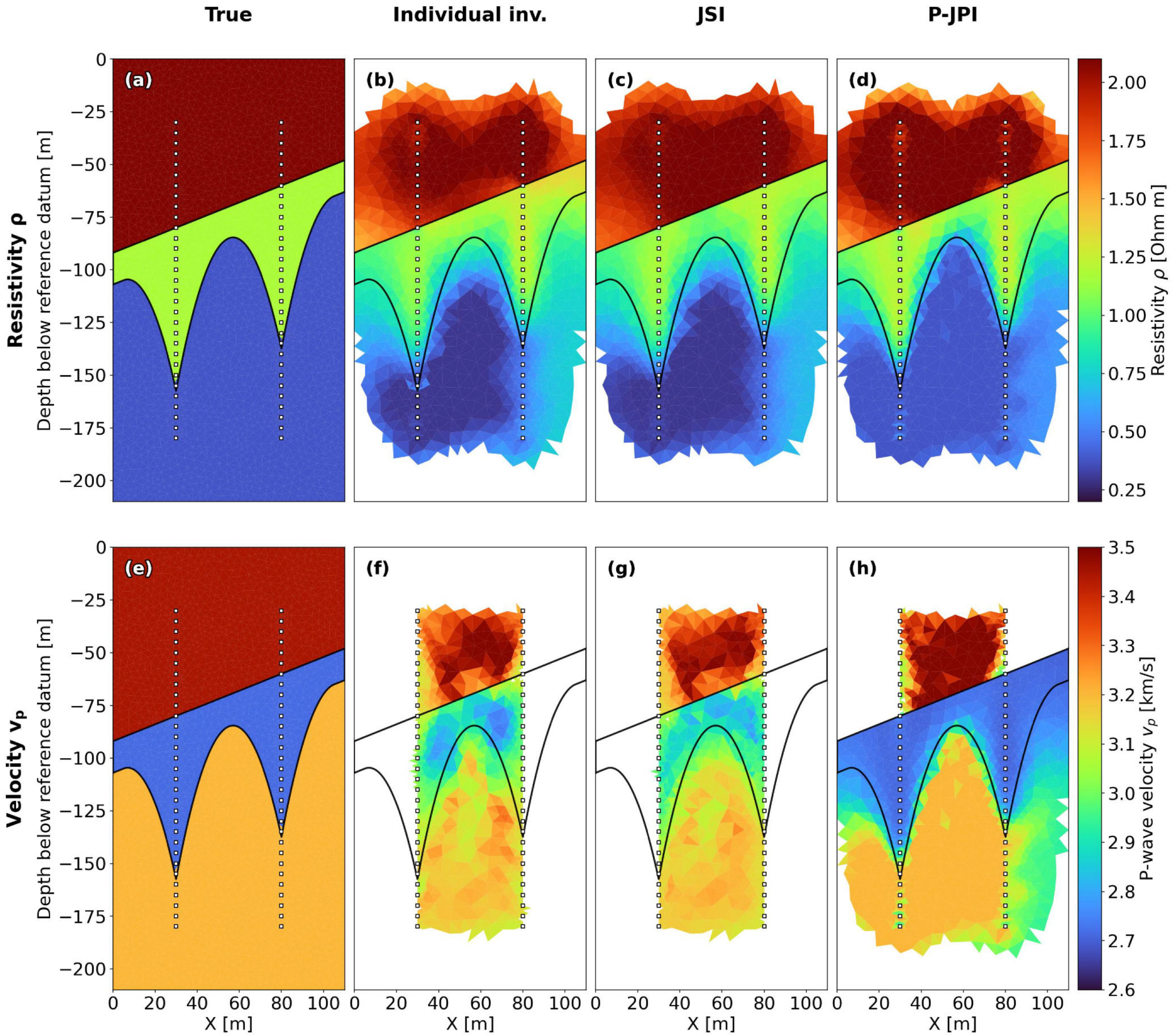

Figure 8. True model parametrization together with tomograms from the individual geophysical inversions, JSI, and P-JPI. Rows show resistivity ρ and P-wave velocity v_p. Columns show the true models, and the tomograms from standalone geophysical inversions, JSI and P-JPI. Sensor positions are indicated by white squares. The outline of the CO_2-plume is highlighted by a black line. Cells not resolved are displayed in white. For the P-JPI, cells in the trusted region (reservoir) are resolved if they are resolved by either ERT or TT seismics. In the untrusted region cells are considered to be resolved, if they are resolved by the their respective method.

estimate up to 25 m outside the monitoring borehole setup. Both the CO_2 plume outline and the saturation values are recovered very precisely. In contrast to the standalone inversions, the P-JPI provides a unique saturation model for the reservoir, making the interpretation unambiguous.

4 DETECTION OF ZONES WITH FAULTY PETROPHYSICAL RELATIONS

The P-JPI relies on prior knowledge of where the petrophysical relationships are valid. In practice, this information is often unavailable or highly uncertain. Therefore, identifying regions in which the petrophysical laws hold or break down is crucial, especially if limited prior information is available or the subsurface is highly heterogeneous.

For a crosshole setup, the data cross-plots in Fig. 4 reveal that certain regions are sensitive only to certain data. Consequently, investigating the data misfit in these cross-plots (see Fig. 6) can indicate regions with high data misfit, which may results from either poor data quality or invalid petrophysical relationships. However, this method provides only a rough estimate of where petrophysical relations break down. Furthermore, it is unclear whether and how this procedure can be generalized to surface or irregular acquisition setups.

In general, regions with inappropriate models are identified through model updates during the inversion process. For petrophysical relations that are valid throughout the full model domain, performing a full joint petrophysical inversion leads to a model that explains both data and therefore no data requests further model updates. In contrast, Fig. 8 shows that if the petrophysical

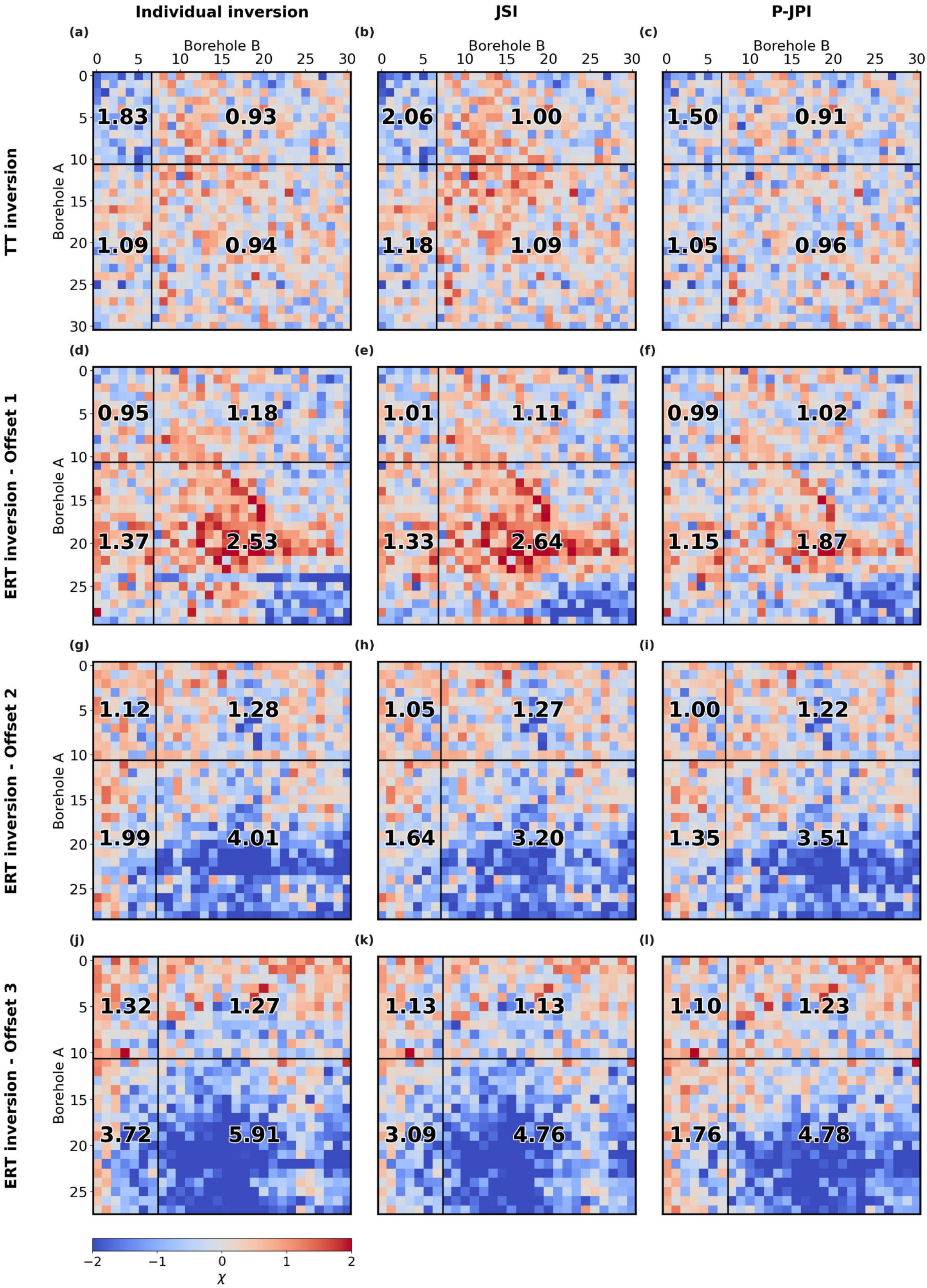

Figure 9. Pointwise data residual shown in cross-plots in multiples of the standard deviation of the added Gaussian noise. Sensors are indexed from top to bottom of the borehole. Columns correspond to a single inversion, that is individual inversions of the ERT and TT data set respectively, JSI and P-JPI. Rows show the data residuals of the traveltime data, and data residuals of the ERT data for fix injection/measurement electrode distance of 1 sensor or 5 m, 2 sensors or 10 m and 3 sensors or 15 m. The cross-plots have been subdivided in four ‘quadrants’ according to the sensitivity of the data to the layer interface and individual χ^2-values have been calculated for each of the quadrants.

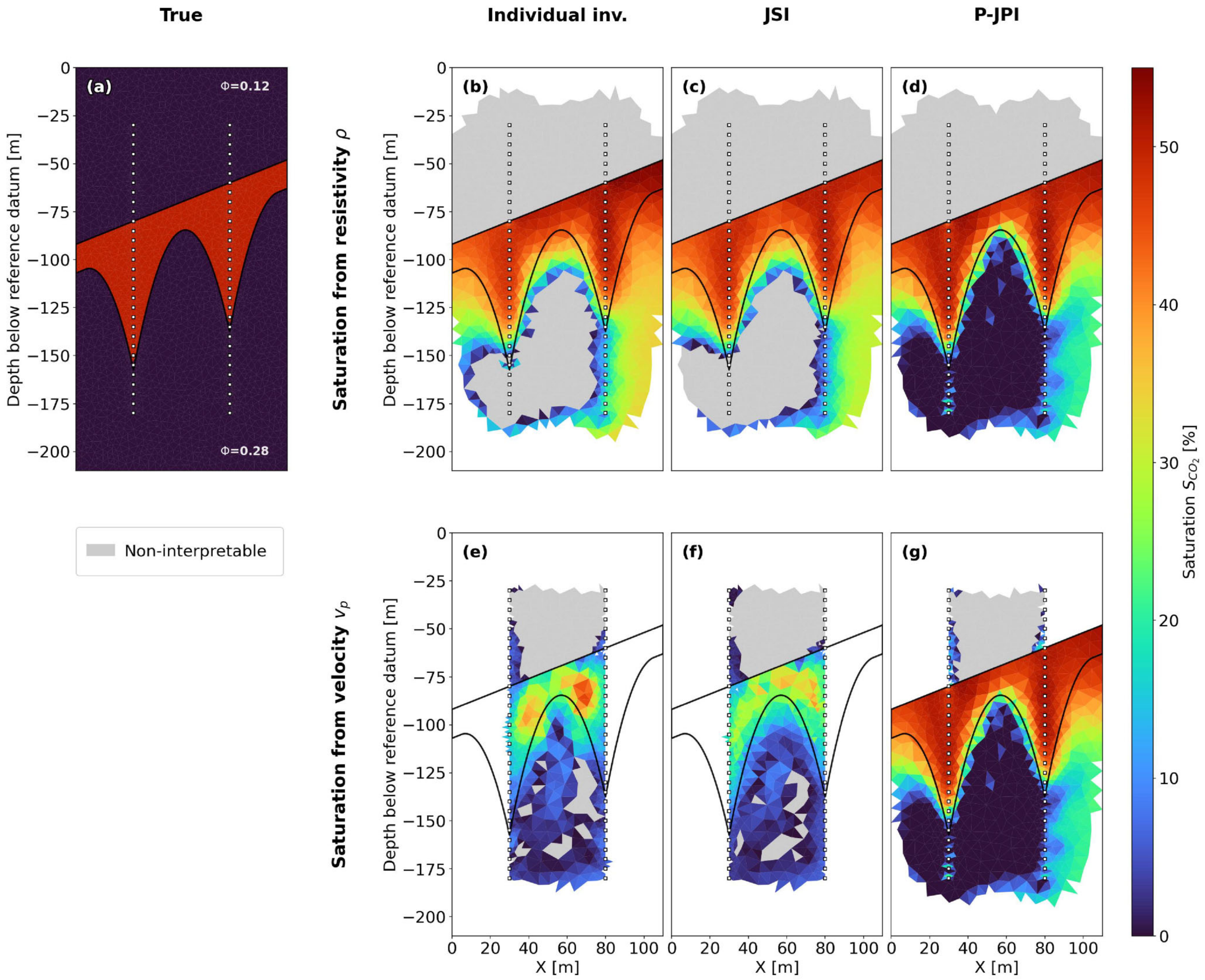

Figure 10. True saturation model together with saturation interpreted from the standalone geophysical inversions, JSI and P-JPI. We show the ground-truth situation (a). Panels (b) to (d) show the saturation interpreted from the resistivity model of the standalone ERT, JSI and mixed saturation/resistivity model of the P-JPI. Panels (e) to (g) show the saturation interpreted from the *P*-wave velocity model of the standalone TT seismics, JSI and the mixed saturation/velocity model of the P-JPI. Sensor positions are indicated by white squares. The outline of the CO_2-plume is highlighted by a black line. Cells not resolved are displayed in white. For the P-JPI, cells in the trusted region (reservoir) are resolved if they are resolved by either ERT or TT seismics. In the untrusted region cells are considered to be resolved, if they are resolved by the their respective method. Cells with geophysical parameter values outside the range of the petrophysical relationship employed cannot be interpreted as saturations and are displayed in grey.

relations are invalid in parts of the domain, the resulting model does not explain both data. Instead, the recovered petrophysical model explains one of the data sets based on the selected data weight, as different petrophysical models are needed to explain the different data, or constitutes a compromise thereof. In this case, both data individually request model updates, which cancel each other out.

We can use this insight to decide whether and where the petrophysical relations hold within the domain. Specifically, we compute model updates independently for each data set. In regions where the petrophysical laws hold, these individual model updates should be similar and disappear in the course of the inversion. In contrast, in regions where the petrophysical laws do not apply, both model updates requested by the individual data will not vanish and differ strongly.

We incorporate this approach in the P-JPI algorithm: In order to avoid decoupling parts of the models in which the petrophysical relationships hold, we first perform conventional joint petrophysical inversion steps until the data fit no longer improves significantly and a compromise model for both data is reached. Only hereafter we allow parts of the model domain to be decoupled. Before each subsequent model update, we assess whether and where the petrophysical laws hold by comparing model updates derived from the individual data. Cells where the difference between both updates exceeds a specified threshold are then decoupled.

To prevent the formation of small, isolated patches, we include a minimum area criterion for both coupled and decoupled regions. For this, we construct a graph based on the mesh and its connectivity, where each cell is represented as a node, and nodes are connected, if their corresponding cells neighbour each other. First, we investigate

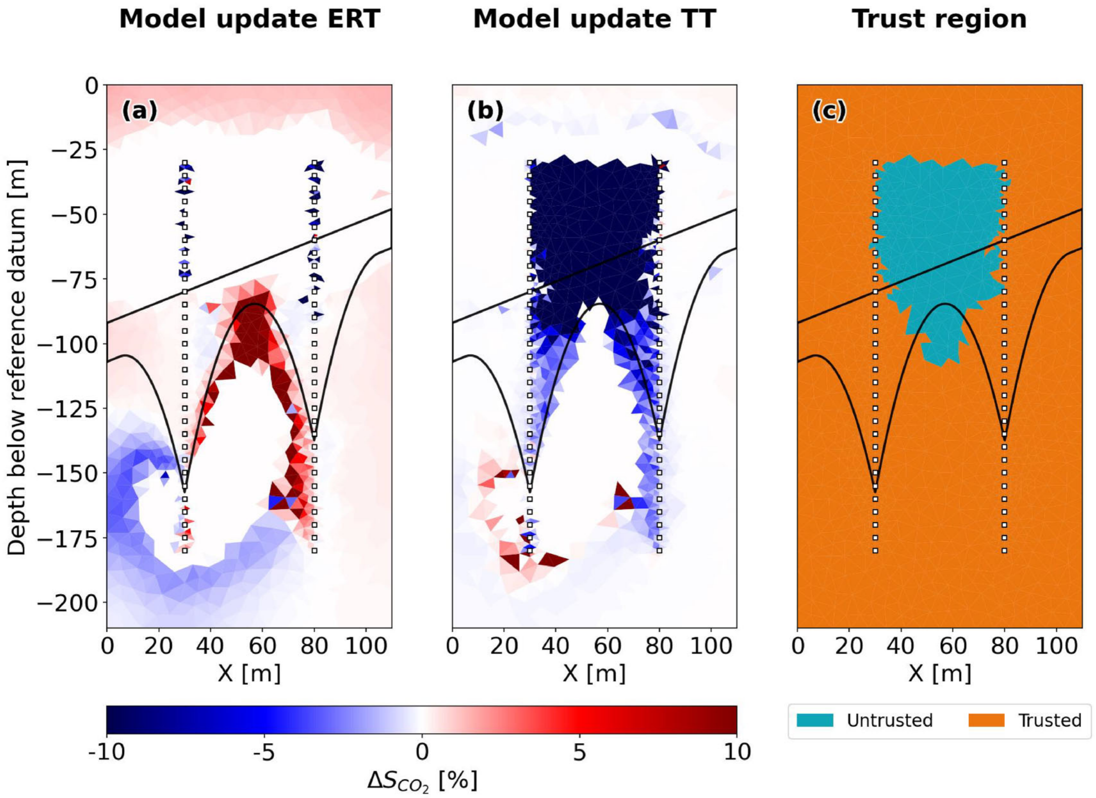

Figure 11. Individual model updates and suggested petrophysical trust region. Panels (a) and (b) show the model updates suggested for the first detection step of the petrophysically trusted region. Panel (c) shows the region of model cells with trusted/untrusted petrophysical relations after the removal of components smaller than 500 m^2.

the size of all connected components, where the models are suggested to be decoupled and decouple only components that exceed the minimum area. Secondly, we calculate all connected components, where the models are suggested to be coupled, and only keep them coupled if they exceed in the minimum area. This approach prevents the occurrence of isolated coupled and decoupled cells.

We apply the P-JPI approach with automatic detection of the petrophysical validity to our synthetic data set. We use a TT-weight of 2.0 and initiate the decoupling process when neither data set improves its respective χ^2 misfit by more than 1 per cent, when the inversion would terminate otherwise. Model cells are decoupled if the difference between individual updates exceeds 9.9 per cent.

Figs 11(a) and (b) display the model updates derived from individual data sets for the first detection step. The model update based solely on the ERT data exhibits only minor updates within the reservoir and no significant updates within the caprock. In contrast, the model update based only on the seismic traveltime data is large within the caprock and the uppermost 20 m of the reservoir, as well as around the location of the CO_2 plume. This observation highlights the trade-offs between the caprock and reservoir models.

The imbalance in the magnitudes of the model updates within the caprock area stems from the TT-weight of 2.0 which tends to favour the ERT-data over the traveltime seismic data (see Fig. 7). As a result, the initial model used to determine the validity of the petrophysical laws is similar to the standalone ERT tomogram, and the inversion based on the ERT data alone suggests only minor updates. In the reservoir, both model updates show significant contributions, indicating that the wrong caprock parameters significantly influence the reservoir model.

Fig. 11(c) shows the final detection result for zones with trusted and untrusted petrophysical relations. Wrong petrophysical relationships are detected in the caprock between the monitoring boreholes and in the upper 20 m of the reservoir, again underscoring the trade-off between the caprock and the reservoir model.

Fig. 12 shows the final saturation tomogram, together with the final velocity and resistivity models. The final saturation tomogram in Fig. 12(a) shows a very accurate recovery of saturations in the reservoir area, where the petrophysical relationships are trusted. In the caprock, the model remains coupled outside the borehole setup, as this area is not sensitive to the traveltime seismic data and the ERT data does not request big model updates. In these areas, the model exhibits high saturation values around 55 per cent. Although these saturation values are generally too small to explain the high resistivity of the caprock, this model tends to fit the ERT data.

The final resistivity and velocity tomograms shown in Figs 12(b) and (c) show a good recovery of the resistivity and *P*-wave velocity models within the borehole setup, as well as outside the borehole setup within the reservoir.

The resistivity model shows a sharper recovery of the CO_2 plume boundaries compared to the geophysical standalone ERT tomograms in Fig. 8(b) and the caprock model is recovered accurately within the borehole setup. Note, however, that the layer boundary is not recovered as accurately compared to the standalone inversion because we assume no structural knowledge about the subsurface and structures are therefore smoothened over the layer boundary. Outside the borehole setup, the resistivity values are significantly lower than the ground truth values, as the domain outside the borehole setup remains coupled and the resistivity values are constrained by the maximum CO_2 saturation of 55 per cent.

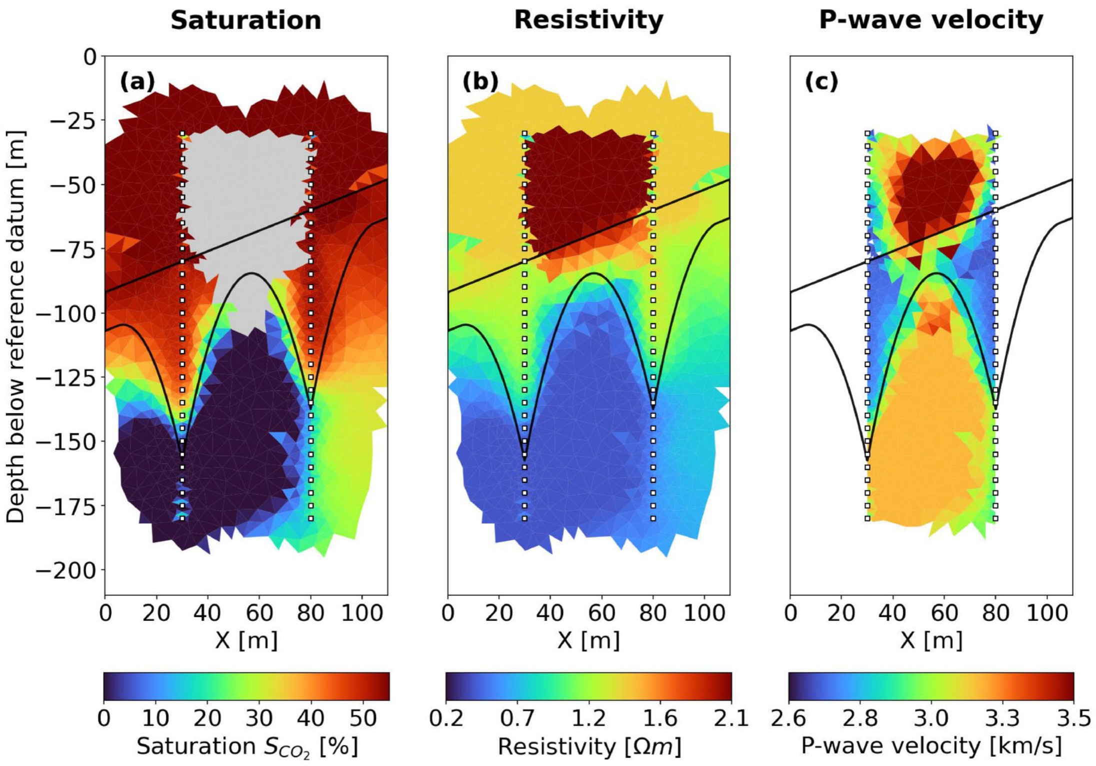

Figure 12. Final saturation model (a), resistivity model (b) and *P*-wave velocity model (c) for the P-JPI with automatic detection of the zones with trusted petrophysical relations. Cells not resolved are displayed in white. Cells with untrusted petrophysical relationship are displayed in grey in the saturation model.

The *P*-wave velocity tomogram also exhibits a good recovery of the caprock parameters and an improved recovery of the CO_2 plume outline and parameters compared to the standalone traveltime seismic tomography shown in Fig. 8(f). Again, the layer boundary appears smeared compared to the standalone tomography as the model is smoothed over the layer boundary.

In summary, the P-JPI with automatic detection provides improved reservoir model recovery compared to the standalone geophysical inversion and a unique saturation model for most parts of the reservoir. Therefore, the P-JPI with automatic detection provides a good solution for the estimation of the CO_2 saturations when no information on the structure of the subsurface and the validity of the petrophysical relations employed is available.

5 DISCUSSION

The synthetic experiments conducted in Section 3 demonstrated that joint inversion techniques are highly advantageous within a CO_2 monitoring scenario, with both individual techniques exhibiting inherent weaknesses. Tomography based only on ERT data provides exact quantitative estimates of the CO_2 saturations, but the structures appear smeared on the tomograms. Tomography based only on seismic traveltime information is capable of providing improved information about the subsurface structure but provides only poor, effectively unusable quantitative estimates between the boreholes.

Applying a conventional JPI scheme showed that coupling the models petrophysically constitutes a strong quantitative (and hence structural) coupling that leads to greatly improved tomograms for regions with valid petrophysical relationships. However, if the petrophysical relationships are not valid in the entire model domain, major artefacts are introduced in regions where the petrophysical relationships hold and individual or joint petrophysical inversion becomes infeasible. This statement is also supported by the χ^2 values in Table 2, which indicate that both the individual and joint petrophysical inversion exhibit very high misfit values.

Artefacts arising from wrong petrophysical relationships can be classified into two categories: First, boundary artefacts occur when the correct geophysical parameters cannot be represented by petrophysical parameters, causing the parameters to become trapped at the prescribed boundaries. Secondly, compromise artefacts occur if the geophysical parameters still lie within the range of representable values, but both data need different petrophysical models to explain the respective data. This makes the resulting model highly dependent on the data weight.

Relaxing the joint inversion scheme to a mere structural coupling leads to an excellent data fit (see Table 2) and improved tomograms. However, the traveltime tomogram does not profit of the quantitative information provided by the ERT tomogram. Therefore, JSI results in two very different estimates for the CO_2-saturations, which inhibits a quantitative interpretation of the tomograms. Although this effect can likely be mitigated by using more sensitive imaging techniques like seismic full waveform inversion, petrophysical coupling constitutes the superior coupling technique, whenever applicable.

Our study demonstrates that decoupling the petrophysical model for the caprock while maintaining petrophysical coupling within the reservoir results in a highly accurate and unique saturation model for the reservoir. Moreover, this approach achieves a significantly better fit for both the ERT and seismic data compared to all other JPI inversions, clearly outperforming the standalone geophysical inversions. Therefore, the P-JPI combines the best of both worlds, a quantitatively accurate tomogram with good data fit that is unique wherever the petrophysical relations hold.

Table 2. TT-weight and χ^2 data misfit of different inversion schemes for both ERT and TT data.

	Petrophysical (ind.)	Geophysical (ind.)	JPI	JPI	JPI	JSI	P-JPI
TT-weight	N/A	N/A	0.1	2	10	2	2
ERT	26.23	2.78	27.47	40.32	52.78	1.84	2.15
TT	1.76	1.05	14.97	6.23	4.34	1.14	1.02

Generally, the petrophysically decoupled region should be equipped with cross-gradient constraints, to make the P-JPI a true hybrid method. We tested adding cross-gradient constraints for our synthetic example, but the resulting tomograms were qualitatively similar to those shown in Section 3, since the caprock does not exhibit relevant structures.

The application of the conventional JPI to our synthetic example led to artefacts mainly in the region of faulty petrophysical laws but also significantly influenced the region close to the boundary between caprock and reservoir. However, we expect that this observation cannot be generalised and depends strongly on the acquisition setup. For example, in surface-based acquisition, we expect the effects of partially invalid petrophysical laws to be more severe.

For the P-JPI, prior knowledge of the zones where the petrophysical relations hold and do not hold is required. We showed that zones of invalid petrophysical relationships can be inferred based on multiple geophysical data by analysing the model updates requested by the individual data. For our synthetic case, we could correctly identify the caprock as a zone of invalid petrophysical relationships. Unfortunately, the trade-off between the caprock and reservoir models did not allow us to precisely determine the boundary, and significant parts of the reservoir were also decoupled. We expect that the detection of these zones can be improved by using more advanced strategies, e.g. decoupling the model before a full compromise model is reached to reduce the effect of artefacts and local minima as well as using cross-gradients constraints to enforce updates with similar structure.

Recovery of regions with invalid petrophysical laws, indicated by divergent model updates suggested by the individual methods, provides information only for regions in which both data are sensitive. However, in the case of boundary artefacts—that is, when the petrophysical parameters cannot represent the true geophysical parameters—it is possible to infer the invalidity of the petrophysical relationships. In such cases, a standalone petrophysical inversion does not propose model updates, as the parameters are constrained by the log-barrier function. In contrast, a standalone geophysical inversion will suggest non-trivial model updates because the geophysical parameters are not adjusted to fit the recorded data. Therefore, regions with invalid petrophysical relations constrained at the parameter boundaries can be identified by comparing the model updates suggested by standalone petrophysical and geophysical inversions. However, this remains a subject for future research.

In practical applications, petrophysical parameters are often only of interest in some parts of the domain. The P-JPI offers a suitable approach for a target-oriented petrophysical inversion. For this, the models are only coupled for the target region, where a coherent petrophysical model is enforced, whereas the other regions are merely modelled geophysically. This approach then limits the influence of variations of the hyperparameters of the petrophysical laws and prevents the occurrence of artefacts thereof.

6 CONCLUSION

Joint inversion techniques have the potential to drastically improve subsurface imaging compared to single-data inversions. The combination of ERT and seismic traveltime data in the context of estimating CO_2 saturations proved to be very advantageous, with ERT providing accurate quantitative information and seismic data providing accurate structural information. Employing petrophysical coupling proved to provide superior tomograms but relies on accurate petrophysical laws for the full model domain.

We showed that wrong petrophysical laws lead to artefacts that strongly depend on the data weighting, as well as to structured misfit in the data. The P-JPI method provides a hybrid approach, combining petrophysical and structural coupling, to create accurate tomograms when the petrophysical laws are only valid in some parts of the model domain. For this, the geophysical models are petrophysically coupled in regions where the petrophysical laws hold, and merely structurally coupled, wherever the petrophysical laws are invalid. This approach is able to provide a unique petrophysical subsurface model whenever possible, while providing a good data fit.

The P-JPI enables the application of joint petrophysical inversion even if the petrophysical laws are not known in the full model domain or petrophysical parameters only of interest in a subdomain. Finally we showed, that petrophysical joined inversion provides means, to quantify regions with invalid petrophysical laws. By combining the benefits of structural and petrophysical coupling, our study contributes to improved quantitative subsurface imaging on multiple geophysical modalities.

ACKNOWLEDGMENTS

The authors thank our colleagues Kathrin Behnen, Nino Menzel and Andrea Balza Morales for helpful discussions regarding the methodology and the implementation. This project has received funding from the European Union's Horizon 2020 research and innovation programme under the Marie Sklodowska-Curie grant agreement No 956965.

The authors contributions are: Conceptualization: HS, FW; Methodology: HS; Writing—original draft: HS; Writing—review and editing: FW, HM.

DATA AVAILABILITY

The Python code developed for this work is openly available under Creative Commons Attribution 4.0 license at GitHub: https://github.com/soehag/pjpi.

REFERENCES

Abubakar, A., Gao, G., Habashy, T. M. & Liu, J., 2012. Joint inversion approaches for geophysical electromagnetic and elastic full-waveform data, *Inverse Probl.,* **28**(5), 055016.

Archie, G., 1942. The electrical resistivity log as an aid in determining some reservoir characteristics, *Trans. AIME,* **146**(01), 54–62.

Brie, A., Pampuri, Marsala, A. & Meazza, O., 1995. Shear sonic interpretation in gas-bearing sands, in *SPE Annual Technical Conference and Exhibition, Dallas, Texas,* Society of Petroleum Engineers, Inc.. doi:

Crestel, B., Stadler, G. & Ghattas, O., 2019. A comparative study of structural similarity and regularization for joint inverse problems governed by PDEs, *Inverse Probl.,* **35**(2), 024003..

Domenzain, D., Bradford, J. & Mead, J., 2020. Joint inversion of full-waveform ground-penetrating radar and electrical resistivity data: Part 1, *Geophysics,* **85**(6), H97–H113.

Förster, A., Norden, B., Zinck-Jørgensen, K., Frykman, P., Kulenkampff, J., Spangenberg, E., Erzinger, J., Zimmer, M., Kopp, J., Borm, G., Juhlin, C., Cosma, C.-G. & Hurter, S., 2006. Baseline characterization of the CO2SINK geological storage site at Ketzin, Germany, *Environ. Geosci.,* **13**(3), 145–161.

Gallardo, L. A. & Meju, M. A., 2003. Characterization of heterogeneous near-surface materials by joint 2D inversion of dc resistivity and seismic data: characterization of heterogeneous near-surface materials, *Geophys. Res. Lett.,* **30**(13) .

Gassmann, F., 1951. Ueber die Elastizität poröser Medien, *Zürich, Institut für Geophysik,* Institut für Geophysik - Eidgenössische Technische Hochschule(Zürich); Mitteilungen 17.

Heincke, B., Jegen, M., Moorkamp, M., Hobbs, R. W. & Chen, J., 2017. An adaptive coupling strategy for joint inversions that use petrophysical information as constraints, *J. Appl. Geophys.,* **136,** 279–297.

Ivanova, A., Kashubin, A., Juhojuntti, N., Kummerow, J., Henninges, J., Juhlin, C., Lüth, S. & Ivandic, M., 2012. Monitoring and volumetric estimation of injected CO_2 using 4D seismic, petrophysical data, core measurements and well logging: a case study at Ketzin, Germany, *Geophys. Prospect.,* **60**(5), 957–973.

Jordi, C., Doetsch, J., Günther, T., Schmelzbach, C., Maurer, H. & Robertsson, J. O. A., 2020. Structural joint inversion on irregular meshes, *Geophys. J. Int.,* **220**(3), 1995–2008..

Kummerow, J. & Spangenberg, E., 2011. Experimental evaluation of the impact of the interactions of CO_2 -SO_2, brine, and reservoir rock on petrophysical properties: A case study from the Ketzin test site, Germany, *Geochem. Geophys. Geosyst.* **12**(5), 2010GC003469.

Moser, T. J., 1991. Shortest path calculation of seismic rays, *Geophysics,* **56**(1), 59–67.

Norden, B., F”orster, A., Vu-Hoang, D., Marcelis, F., Springer, N. & Le Nir, I., 2010. Lithological and Petrophysical Core-Log Interpretation in CO2SINK, the European CO_2 Onshore Research Storage and Verification Project, *SPE Reservoir Eval. Eng.,* **13**(02), 179–192.

Qin, T., Bohlen, T. & Pan, Y., 2024. Indirect joint petrophysical inversion of shallow-seismic and multi-offset ground-penetrating radar field data, *Geophys. J. Int.,* **237**(2), 974–988.

Rücker, C., Günther, T. & Spitzer, K., 2006. Three-dimensional modelling and inversion of dc resistivity data incorporating topography - I. Modelling, *Geophys. J. Int.,* **166**(2), 495–505.

Rücker, C., Günther, T. & Wagner, F. M., 2017. pyGIMLi: An open-source library for modelling and inversion in geophysics, *Comput. Geosci.,* **109,** 106–123.

Wagner, F. M., Mollaret, C., Günther, T., Kemna, A. & Hauck, C., 2019. Quantitative imaging of water, ice and air in permafrost systems through petrophysical joint inversion of seismic refraction and electrical resistivity data, *Geophys. J. Int.,* **219**(3), 1866–1875.

APPENDIX A: TRANSFORMED JACOBIAN MATRICES

We derive an explicit formula for the transformed Jacobian matrix $\tilde{\boldsymbol{J}}$ for both the petrophysical and the geophysical case. Without loss of generality, we derive the formulation for the ERT measurement as the formulation for the seismic traveltime data follows by replacing the forward operator, petrophysical law and log-barrier transformation with the corresponding seismic equivalents. For the petrophysical case, assume a fully petrophysically coupled model, that is, the full domain is parametrized by saturations. We denote the ERT forward operator by $\mathcal{F}^E$ and obtain the relationship $\tilde{\boldsymbol{m}} \xrightarrow{\varphi^{-1}} \boldsymbol{m} \xrightarrow{p^E} \boldsymbol{\rho} \xrightarrow{\mathcal{F}^E} \boldsymbol{d}^{\boldsymbol{E}}_{\mathbf{obs}}$. By the chain rule, we have

$$\frac{\partial \boldsymbol{d}^{\boldsymbol{E}}_{\mathbf{obs}}}{\partial \tilde{\boldsymbol{m}}} = \frac{\partial \boldsymbol{d}^{\boldsymbol{E}}_{\mathbf{obs}}}{\partial \boldsymbol{\rho}} \frac{\partial \boldsymbol{\rho}}{\partial \boldsymbol{m}} \frac{\partial \boldsymbol{m}}{\partial \tilde{\boldsymbol{m}}}. \tag{A1}$$

The derivatives of the observed data with respect to the resistivity model $\frac{\partial \boldsymbol{d}^{\boldsymbol{E}}_{\mathbf{obs}}}{\partial \boldsymbol{\rho}}$ are obtained from the numerical solver, as explained in Section 2.1. The derivative of the geophysical model with respect to the petrophysical model $\frac{\partial \boldsymbol{\rho}}{\partial \boldsymbol{m}}$ and the derivative of the petrophysical model with respect to the (inverse) log-barrier transformation $\frac{\partial \boldsymbol{m}}{\partial \tilde{\boldsymbol{m}}}$ are obtained from a finite difference approximation. The final Jacobian matrix follows as

$$\tilde{\boldsymbol{J}} = \begin{pmatrix} \frac{\partial d^E_{\mathrm{obs},1}}{\partial \tilde{m}_1} & \cdots & \frac{\partial d^E_{\mathrm{obs},1}}{\partial \tilde{m}_N} \\ \vdots & \ddots & \vdots \\ \frac{\partial d^E_{\mathrm{obs,M}}}{\partial \tilde{m}_1} & \cdots & \frac{\partial d^E_{\mathrm{obs,M}}}{\partial \tilde{m}_N} \end{pmatrix} = \begin{pmatrix} \frac{\partial d^E_{\mathrm{obs},1}}{\partial \rho_1} \frac{\partial \rho_1}{\partial m_1} \frac{\partial m_1}{\partial \tilde{m}_1} & \cdots & \frac{\partial d^E_{\mathrm{obs},1}}{\partial \rho_N} \frac{\partial \rho_N}{\partial m_N} \frac{\partial m_N}{\partial \tilde{m}_N} \\ \vdots & \ddots & \vdots \\ \frac{\partial d^E_{\mathrm{obs,M}}}{\rho_1} \frac{\partial \rho_1}{\partial m_1} \frac{\partial m_1}{\partial \tilde{m}_1} & \cdots & \frac{\partial d^E_{\mathrm{obs,M}}}{\partial \rho_N} \frac{\partial \rho_N}{\partial m_N} \frac{\partial m_N}{\partial \tilde{m}_N}. \end{pmatrix} \tag{A2}$$

As the last two partial derivatives are constant throughout each column, we can rewrite eq. (A2) by matrix multiplication from the right as

$$\tilde{\boldsymbol{J}} = \boldsymbol{G} \cdot \mathrm{diag}\left(\frac{\partial \rho_1}{\partial m_1}, \ldots, \frac{\partial \rho_1}{\partial m_N}\right) \cdot \mathrm{diag}\left(\frac{\partial m_1}{\partial \tilde{m}_1}, \ldots, \frac{\partial m_N}{\partial \tilde{m}_N}\right) \tag{A3}$$

with geophysical Jacobian $\boldsymbol{G} = \frac{\partial \boldsymbol{d}^{\boldsymbol{E}}_{\mathbf{obs}}}{\partial \boldsymbol{\rho}}$.

For the model characterized by geophysical quantities together with log-barrier constraints, we obtain the analogue relation $\tilde{\boldsymbol{m}} \xrightarrow{\varphi^{-1}} \boldsymbol{\rho} \xrightarrow{\mathcal{F}^E} \boldsymbol{d}^{\boldsymbol{E}}_{\mathbf{obs}}$. Following the derivations above, the final Jacobian calculates as

$$\tilde{\boldsymbol{J}} = \begin{pmatrix} \frac{\partial d^E_{\mathrm{obs},1}}{\partial \tilde{m}_1} & \cdots & \frac{\partial d^E_{\mathrm{obs},1}}{\partial \tilde{m}_N} \\ \vdots & \ddots & \vdots \\ \frac{\partial d^E_{\mathrm{obs,M}}}{\partial \tilde{m}_1} & \cdots & \frac{\partial d^E_{\mathrm{obs,M}}}{\partial \tilde{m}_N} \end{pmatrix} = \begin{pmatrix} \frac{\partial d^E_{\mathrm{obs},1}}{\partial \rho_1} \frac{\partial \rho_1}{\partial \tilde{m}_1} & \cdots & \frac{\partial d^E_{\mathrm{obs},1}}{\partial \rho_N} \frac{\partial \rho_N}{\partial \tilde{m}_N} \\ \vdots & \ddots & \vdots \\ \frac{\partial d^E_{\mathrm{obs,M}}}{\rho_1} \frac{\partial \rho_1}{\partial \tilde{m}_1} & \cdots & \frac{\partial d^E_{\mathrm{obs,M}}}{\partial \rho_N} \frac{\partial \rho_N}{\partial \tilde{m}_N} \end{pmatrix} \tag{A4}$$

and

$$\tilde{\boldsymbol{J}} = \boldsymbol{G} \cdot \mathrm{diag}\left(\frac{\partial \rho_1}{\partial \tilde{m}_1}, \ldots, \frac{\partial \rho_N}{\partial \tilde{m}_N}\right). \tag{A5}$$

In the case of a partly decoupled parametrization, the final Jacobian is compiled column by column.

APPENDIX B: CROSS-GRADIENT CONSTRAINTS FOR UNSTRUCTURED MESHES

The derivation of the cross-gradient constraints is similar to the one presented in C. Jordi et al. (2020) but has been developed independently of this publication. Therefore, we here provide a short derivation and point out the major differences to the approach presented in C. Jordi et al. (2020).

Calculating the gradient for the resistivity $\boldsymbol{\rho}$ and *P*-wave velocity $\boldsymbol{v_p}$ model requires a discretization of the spatial gradient operator. For regular meshes, this can be achieved by standard finite-difference approaches, which are based on Taylor approximations. This approach can be straightforwardly generalized to unstructured meshes: For a general model $\boldsymbol{m}$, a cell with index c and cell centre $\boldsymbol{x_c}$, the first-order Taylor approximation reads $\boldsymbol{m}(x) \sim \boldsymbol{m}(c) + \nabla \boldsymbol{m}(c)^T (x - \boldsymbol{x_c})$ for all x in the neighbourhood of $\boldsymbol{x_c}$. For two spatial dimensions, the model gradient $\nabla \boldsymbol{m}$ consists of two components, which can be determined using a least-squares approach. This approach differs from C. Jordi et al. (2020) in that we directly use the Taylor expansion instead of a generalized linear fit, which is not fixed at $\boldsymbol{x_c}$ to $m(c)$, but rather contains an additional offset term.

We choose k neighbour cells $n_1, \ldots, n_k$ with cell centres $\boldsymbol{x_1}, \ldots, \boldsymbol{x_k}$ and collect the Taylor expansions as a system of equations.

$$\begin{pmatrix} — (\boldsymbol{x_1} - \boldsymbol{x_c}) — \\ \vdots \\ — (\boldsymbol{x_k} - \boldsymbol{x_c}) — \end{pmatrix} \nabla \boldsymbol{m}(x) = \begin{pmatrix} \boldsymbol{m}(n_1) - \boldsymbol{m}(c) \\ \vdots \\ \boldsymbol{m}(n_k) - \boldsymbol{m}(c) \end{pmatrix} =: \boldsymbol{D_c} \boldsymbol{\Delta m}(x) \quad \text{(B1)}$$

We define the spatial gradient by the least-squares solution of eq. (B1), more specifically as $\nabla \boldsymbol{m}(c) = (\boldsymbol{D_c}^T \boldsymbol{D_c})^{-1} \boldsymbol{D_c} \boldsymbol{\Delta m}(c) =: \boldsymbol{E_c} \boldsymbol{\Delta m}(c)$. In contrast to the approach of C. Jordi et al. (2020), we do not employ a space-dependent weighting for the solution of the least-squares problem.

The discretization operator $\boldsymbol{D_c}$ and its least-squares solution operator $\boldsymbol{E_c}$ depend only on the chosen neighbours and the geometry of the mesh and can therefore be calculated in advance once and stored. For a 2-D model, this system is non-singular, if at least two neighbour cells are considered, which are not aligned with respect to the cell centre $\boldsymbol{x_c}$. However, we recommend the use of at least three neighbour cells for numerical stability.

By eq. (B1), the spatial gradient depends linearly on the model itself. We can now calculate the sensitivities of the cross-gradient term with respect to the underlying models in two ways: either expanding the right-hand side or deriving explicit sensitivities directly from the least-squares representation.

First, we expand the right hand side and write $\boldsymbol{\Delta m}(c)$ as a function of the full model vector $\boldsymbol{m}$. This yields the following:

$$\boldsymbol{\Delta m}(c) = \boldsymbol{V m} \text{ with } \boldsymbol{V}_{i,j} = \begin{cases} 1, & \text{for } j = n_i \\ -1, & \text{for } j = c \\ 0, & \text{else} \end{cases} \quad \text{(B2)}$$

and the spatial gradient follows as $\nabla \boldsymbol{m}(c) = \boldsymbol{\tilde{D}_c V m} =: \boldsymbol{E_c m}$ with the sparse matrix $\boldsymbol{E_c}$.

The discretized cross-gradient term of the resistivity and P-wave velocity model can then be written as $\nabla \boldsymbol{\rho}(x) \times \nabla \boldsymbol{v_p}(x) = (\boldsymbol{E_c \rho} \times \boldsymbol{E_c v_p})(x)$. By basic properties of the cross-product the sensitivities with respect to the model vector follow as

$$\begin{aligned} \frac{\partial \left(\nabla \boldsymbol{\rho} \times \nabla \boldsymbol{v_p} \right)}{\partial \boldsymbol{\rho}}(c) &= \frac{\partial \nabla \boldsymbol{\rho}}{\partial \boldsymbol{\rho}}(c) \times \nabla \boldsymbol{v_p}(c) + \nabla \boldsymbol{\rho}(c) \times \frac{\partial \nabla \boldsymbol{v_p}}{\partial \boldsymbol{\rho}}(c) \\ &= \boldsymbol{E_c} \times \nabla \boldsymbol{v_p}(c) \text{ and} \end{aligned} \quad \text{(B3)}$$

$$\begin{aligned} \frac{\partial \left(\nabla \boldsymbol{\rho} \times \nabla \boldsymbol{v_p} \right)}{\partial \boldsymbol{v_p}}(c) &= \frac{\partial \nabla \boldsymbol{\rho}}{\partial \boldsymbol{v_p}}(c) \times \nabla \boldsymbol{v_p}(c) + \nabla \boldsymbol{\rho}(c) \times \frac{\partial \nabla \boldsymbol{v_p}}{\partial \boldsymbol{v_p}}(c) \\ &= \nabla \boldsymbol{\rho}(c) \times \boldsymbol{E_c} = -\boldsymbol{E_c} \times \nabla \boldsymbol{\rho}(c). \end{aligned} \quad \text{(B4)}$$

Alternatively, sensitivities can be directly derived from the least-squares solution by rewriting the matrix $\boldsymbol{\tilde{D}_c}$ column-wise, by

$$\nabla \boldsymbol{m}(x) = \boldsymbol{\tilde{D}_c} \boldsymbol{\Delta m}(x) = \begin{pmatrix} | & & | \\ \boldsymbol{\tilde{D}_c^1} & \ldots & \boldsymbol{\tilde{D}_c^k} \\ | & & | \end{pmatrix} \boldsymbol{\Delta m}(x) \quad \text{(B5)}$$

$$= \boldsymbol{m}(n_1) \boldsymbol{\tilde{D}_c^1} + \ldots + \boldsymbol{m}(n_k) \boldsymbol{\tilde{D}_c^k} - \left(\boldsymbol{m}(c) (\boldsymbol{\tilde{D}_c^1} + \ldots + \boldsymbol{\tilde{D}_c^k}) \right). \quad \text{(B6)}$$

The sensitivities therefore directly follow from the matrix $\boldsymbol{E_c}$ as

$$\begin{aligned} \frac{\partial \left(\nabla \boldsymbol{\rho} \times \nabla \boldsymbol{v_p} \right)}{\partial \boldsymbol{\rho_j}}(c) &= \frac{\partial \nabla \boldsymbol{\rho}}{\partial \boldsymbol{\rho_j}}(c) \times \nabla \boldsymbol{v_p}(c) \\ &= \begin{cases} -(\boldsymbol{\tilde{D}_c^1} + \ldots + \boldsymbol{\tilde{D}_c^k}) \times \nabla \boldsymbol{v_p}(c), & \text{for } j = c \\ \boldsymbol{\tilde{D}_c^i} \times \nabla \boldsymbol{v_p}(c), & \text{for } j = n_i \\ 0, & \text{else} \end{cases} \end{aligned} \quad \text{(B7)}$$

$$\begin{aligned} \frac{\partial \left(\nabla \boldsymbol{\rho} \times \nabla \boldsymbol{v_p} \right)}{\partial \boldsymbol{v_{p,j}}}(c) &= \nabla \boldsymbol{\rho}(c) \times \frac{\partial \nabla \boldsymbol{v_p}}{\partial \boldsymbol{v_{p,j}}}(c) \\ &= \begin{cases} -\nabla \boldsymbol{\rho}(c) \times (\boldsymbol{\tilde{D}_c^1} + \ldots + \boldsymbol{\tilde{D}_c^k}), & \text{for } j = c \\ \nabla \boldsymbol{\rho}(c) \times \boldsymbol{\tilde{D}_c^i}, & \text{for } j = n_i \\ 0, & \text{else} \end{cases} . \end{aligned} \quad \text{(B8)}$$

APPENDIX C: ELECTRODE CONFIGURATIONS

The electrodes for the ERT were placed with three different, but fixed, offsets of 5, 10 and 15 m. In all cases, the first current electrode was positioned in the left borehole, and the first potential measurement electrode was placed at the specified offset below it. Similarly, the second current electrode was positioned in the right borehole, with the second potential measurement electrode placed below it at the same offset. Both electrode pairs were then moved independently along the boreholes while maintaining the fixed offset.

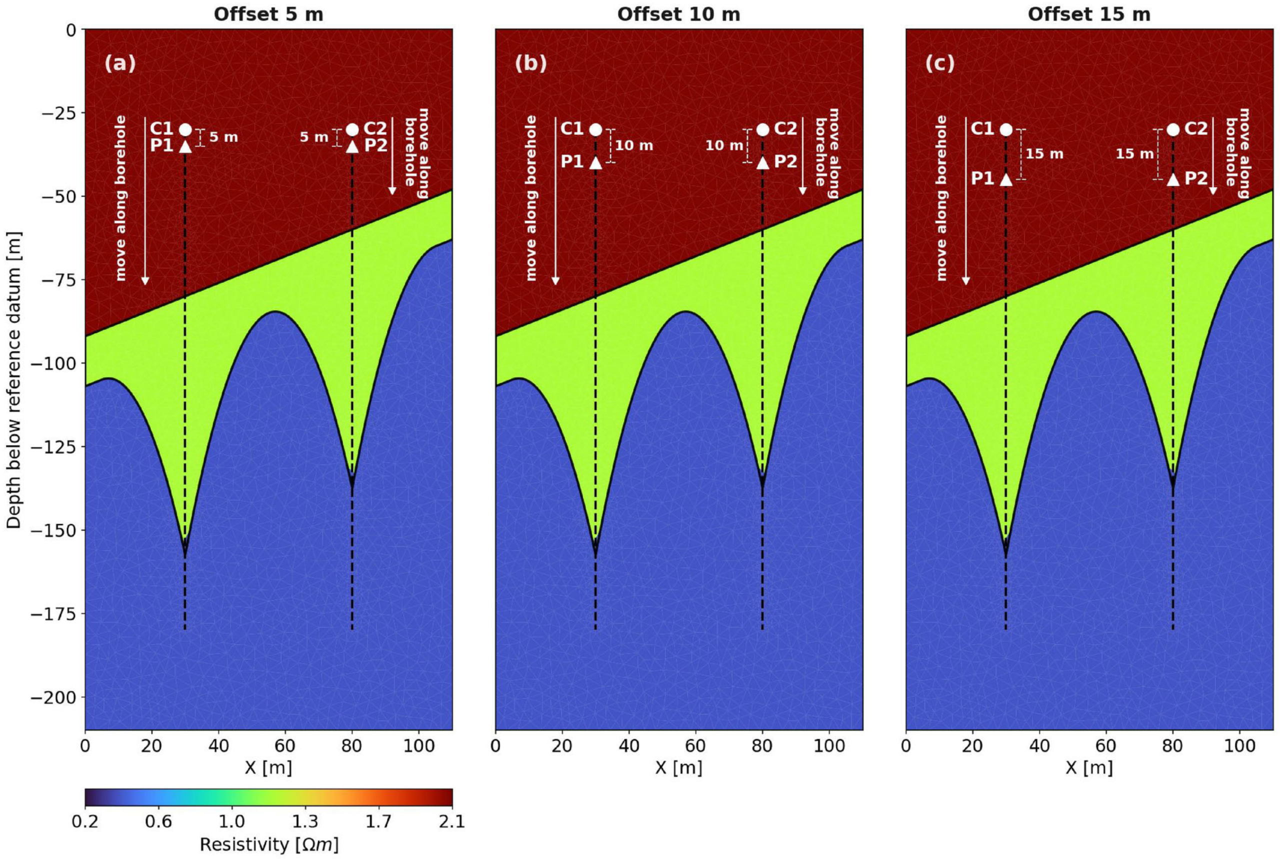

Figure C1. Electrode configurations with fixed offset of 5 m (a), 10 m (b), 15 m (c) superimposed on the true resistivity model.